



THE HONG KONG
POLYTECHNIC UNIVERSITY

香港理工大學

Pao Yue-kong Library

包玉剛圖書館

Copyright Undertaking

This thesis is protected by copyright, with all rights reserved.

By reading and using the thesis, the reader understands and agrees to the following terms:

1. The reader will abide by the rules and legal ordinances governing copyright regarding the use of the thesis.
2. The reader will use the thesis for the purpose of research or private study only and not for distribution or further reproduction or any other purpose.
3. The reader agrees to indemnify and hold the University harmless from and against any loss, damage, cost, liability or expenses arising from copyright infringement or unauthorized usage.

If you have reasons to believe that any materials in this thesis are deemed not suitable to be distributed in this form, or a copyright owner having difficulty with the material being included in our database, please contact lbsys@polyu.edu.hk providing details. The Library will look into your claim and consider taking remedial action upon receipt of the written requests.

**Fabrication and Optical Characterization of
Epitaxial Strontium Barium Niobate Films
for Waveguide Applications**

**Submitted by
LANG Zhong**

**A Thesis Submitted in Partial Fulfillment of the
Requirements for the Degree of Master of Philosophy in
Applied Physics**

At

**The Department of Applied Physics
The Hong Kong Polytechnic University**

October, 2006

Certificate of Originality

I hereby declare that this thesis is my own work and that, to the best of my knowledge and belief, it reproduces no material previously published or written nor material which has been accepted for the award of any other degree or diploma, except where due acknowledgement has been made in the text.

_____ (Signed)

LANG ZHONG (Name of student)



ABSTRACT

$\text{Li}_x\text{Ni}_{1-x}\text{O}$ (LNO) films with $x = 0.15, 0.20, 0.25, 0.30, 0.40, 0.50$ and 0.60 on (001) MgO substrates were fabricated by pulsed laser deposition (PLD). X-ray diffraction (XRD), scanning electron microscopy (SEM) and atomic force microscopy (AFM) were employed to characterize the structural properties of these films; while the optical transmittance (OT) measurement and prism coupling technique were used to measure their optical properties. Our results showed that, above the deposition temperature of $600\text{ }^\circ\text{C}$, all of the LNO films exhibited single phase crystalline structure. They were c -axis oriented with cubic structure, although some very weak peaks, which were identified as the Li_2O phase, were observed from the XRD profiles of the LNO50 and LNO60 films. The LNO films were cube-on-cube grown on MgO substrates with an in-plane epitaxial relationship of (001) LNO || (001) MgO. X-ray photoelectron spectroscopy (XPS) results showed that the Li contents of the films were proportional to the initial Li contents of the targets. The values of the Li content of the films were approximately 20% of the initial Li contents due to Li evaporation during the fabrication process. The LNO films with different Li concentrations showed no remarkable difference in the shape of the OT spectra.



Transmittance of about 40% in the visible range was obtained from LNO40 films. The optical band-gap energy of LNO was found to be in the range of 3.16~3.21 eV. Refractive indices of 1.75-2.0 for the LNO films were measured by spectroscopic ellipsometry. Among all the LNO films, the LNO40 film deposited at 600 °C was found to possess the lowest resistivity of 0.132 Ω·cm. Based on this consideration, LNO40 films were used as both a transparent as well as conducting electrode in this project.

High quality strontium barium niobate (SBN)/LNO thin films were epitaxially grown on (001) MgO substrates using a two-step PLD process. Their structural properties and OT, waveguide properties and electrical conductivity were investigated. The excellent crystalline SBN and LNO films with heteroepitaxial relationship of (100) SBN || (310) LNO/MgO and (100) SBN || (350) LNO/MgO were obtained. SEM results showed that the heterostructure possessed good structural qualities both in the surface and cross-section morphologies. Both the OT and resistivity measurements indicated that our two-step PLD process efficiently increased the transmission of the LNO films from 40% to 65% meanwhile the resistivity was only slightly increased. The transverse electric and transverse magnetic guided modes of SBN films



deposited on MgO substrates were measured by a coupling prism technique.

The ordinary refractive index n_o (n_{TE}) and the extraordinary refractive index n_e (n_{TM}) of SBN film were calculated to be 2.1843 and 2.1684, respectively. The thickness of SBN films obtained by the coupling prism technique was in a good agreement with our SEM results. A propagation loss of 3.45 dB/cm was determined in our SBN waveguide structures.

Epitaxial SBN films have not been successfully grown directly on Si substrates due to a large lattice mismatch. In order to overcome this problem, thin layers of TiN and MgO were used as buffer layers between SBN and Si in our studies. In our work, SBN/MgO/TiN heterostructures were successfully grown on (001) Si substrates by PLD method. Single phase MgO, TiN and SBN layers were *c*-axis oriented. The MgO and TiN are cubic while SBN has a tetragonal structure. All of the films were grown with a cube-on-cube mode and the in-plane orientation relationship between the SBN films, MgO/TiN layers and Si substrates can be described as (110) SBN || (100) MgO/TiN || (100) Si. The SEM micrographes showed that the surfaces were smooth and crack-free. The film thicknesses of each layer were obtained from the SEM cross-sectional micrographs. The waveguide properties were measured by using a prism



coupler. The ordinary refractive index n_o (n_{TE}) and the extraordinary refractive index n_e (n_{TM}) of SBN film were calculated to be 2.0393 and 2.0025, respectively.



PUBLICATIONS

Z. Lang, C. L. Mak and K. H. Wong, Growth of epitaxial strontium barium niobate/lithium nickel oxide heterostructure on (100) MgO substrates using a two-step pulsed laser deposition process, *Proceedings of Symposium J, European Materials Research Society 2006 Spring Meeting*.



ACKNOWLEDGEMENTS

I would like to acknowledge Dr. C. L. Mak for his supervision in the past two years. I specially thank Dr K. H. Wong and Dr. C. W. Leung for their helps and suggestions in many experiments.

I would like to thank Miss Yoyo Yeung and Mr. M. N. Yeung for their supports in many characterization measurements.

I also would like to thank Miss C. Y. Lam, Miss L. Zhuang, Mr. W. C. Liu, Mr D. Y. Wang, Mr. M. K. Sze, Mr. T. Y. Yum, Mr. W. F. Wong and Mr. W. L. Sin.

They have given me many helps and suggestions through my experiments.



Table of Contents

ABSTRACT	i
PUBLICATIONS	v
ACKNOWLEDGEMENTS	vi
Table of Content	vii
 Chapter 1	
 Introduction	
1.1 Background	1
1.2 Strontium Barium Niobate (SBN)	3
1.3 Pulsed Laser Deposition	7
1.3.1 History of Pulsed Laser Deposition	8
1.3.2 Mechanism of Pulsed Laser Deposition	9
1.3.3 The Three Stages of Pulsed Laser Deposition Process	10
1.3.3.1 Laser-Target Interaction	10
1.3.3.2 Target to Substrate Gas Phase Transportation	10
1.3.3.3 Nucleation and Film Growth	11
1.3.4 Advantage and Disadvantage of Pulsed Laser Deposition	12
1.3.4.1 Advantage of Pulsed Laser Deposition	12



1.3.4.2	Disadvantage of Pulsed Laser Deposition	13
1.4	Outline of Thesis	14
Chapter 2		
Optical Waveguides		
2.1	History of Optical Waveguides	17
2.2	Waveguides Concept	19
2.2.1	Total Internal Reflection	19
2.2.2	Slab and Channel Waveguides	21
2.3	Advantages of Optical Waveguides	23
Chapter 3		
Experimental		
3.1	Sample Fabrication	25
3.1.1	Pulsed Laser Deposition	25
3.1.2	Target Fabrication	29
3.1.3	Substrate Preparation	30
3.1.4	Deposition Process	30
3.2	Characterization Instruments	32
3.2.1	X-ray Diffraction (XRD)	32
3.2.2	X-ray Photoelectron Spectroscopy (XPS)	38



3.2.3	Scanning Electron Microscopy (SEM)	42
3.2.4	Atomic-Force Microscopy (AFM)	44
3.2.5	UV-visible Spectrophotometer	46
3.2.6	Prism Coupler	48

Chapter 4

Fabrication and Characterization of LNO and SBN/LNO Films Deposited on (100) MgO Single Crystal Substrates

4.1	Introduction	53
4.2	Fabrication and Characterization of LNO Targets	56
4.2.1	LNO Targets Preparation	56
4.2.2	XRD Characterization	57
4.3	Fabrication and Characterization of LNO Films	60
4.3.1	Fabrication of the LNO Films with Different Li Contents	60
4.3.2	Structural Characterization and Surface Morphology of the LNO Films	62
4.3.3	Characterization of the Lithium Content of the LNO Films	69
4.3.4	Resistivity of LNO Films	70
4.3.5	Optical Transmittance and Refractive Index Measurements of LNO Films	72



4.4	Fabrication and Characterization of SBN/LNO Heterostructures	77
4.4.1	Fabrication of SBN/LNO Films on MgO Substrates	77
4.4.2	Structural Characterization and Surface Morphology of the SBN/LNO Films	78
4.4.3	Conductivity of LNO Layer before and after the Two-Step Deposition Process of SBN Films	85
4.4.4	Optical Transmittance Measurement of the Heterostructures ...	86
4.4.5	Waveguide Properties of the SBN Films	89

Chapter 5

Fabrication and Characterization of SBN Thin Films Grown on (001) Si Substrates Buffered by MgO/TiN Layer

5.1	Introduction	95
5.2	Fabrication and Characterization of SBN/MgO/TiN Heterostructure on (001) Si Substrates	99
5.2.1	Pre-Treatment of Si Substrates	100
5.2.2	Fabrication of SBN/MgO/TiN Heterostructure on (001) Si Substrates	100
5.2.3	Structural Characterization and Surface Morphology of the SBN/MgO/TiN/Si Heterostructure	101



5.2.4	Waveguiding Properties Measurement of Heterostructure by Coupling Prism Technique	107
5.3	Effects of the Film Thickness of MgO Layer on the Optical Loss of the SBN Films	110
Chapter 6		
Conclusions and Future Works		
6.1	Conclusions	112
6.2	Future Works	115
	Reference	118



Chapter 1

Introduction

1.1 Background

Ferroelectric materials are an important class of materials whose main characteristic is the presence of a spontaneous polarization that can be changed with an external electric field. Ferroelectrics include titanates, zirconates and niobates. They can be classified by their structure types. Thin film ferroelectrics offer unique physical characteristics that could dramatically improve the performance of many integrated optic devices. Potential applications include low-voltage electro-optic switching, compact low-threshold gain devices and second-harmonic generation.

In recent year, optical waveguides have attracted much attention for their wide applications in communication systems. They are one of the key components of integrated optic devices. The integration of amplifiers together with other optical components such as splitters, couplers and wavelength division



multiplexers, enables many optical functions to work together on a single chip without optical losses. Therefore, optical waveguides are important fundamental structure for device applications.

Recently, thin-film BaTiO₃ channel waveguides on single crystal MgO substrates have been fabricated. An effective electro-optic coefficient of $\sim 50 \pm 5$ pm/V has been achieved. These BaTiO₃ epitaxial structures offer potential for low-voltage highly confining guided wave electro-optic modulator structures.

This proposed design of hybrid optic and electronic device, typically incorporates a ferroelectric film, a low refractive index buffer layer, and a silicon substrate. Combining these materials with silicon can lead to the integration of devices on the same chip. At present, a fundamental issue in the development of this technology is identifying appropriate ferroelectric- and buffer-layer materials.

In this project, we have fabricated another type of waveguides based on ferroelectric Sr_{1-x}Ba_xNb₂O₆ (SBN). The structural and optical properties of these new waveguides have been investigated.



1.2 Strontium Barium Niobate (SBN)

Fifty years ago, Magneli discovered ferroelectrics of tungsten bronze structure.

The tungsten bronze family is the second largest class of ferroelectric materials

following the perovskite ferroelectrics, which includes niobates such as

(Sr,Ba)Nb₂O₆ (SBN), (Pb,Ba)Nb₂O₆ (PBN) and (Pb,K)Nb₂O₆ (PKN). Among

various ferroelectric materials for optical applications, SBN is one of the most

promising candidates. Initial studies of SBN were carried out on

Czochralski-grown single crystals. [N. Eurgaukar. *et al.*, J. C. Brice. *et al.*]

Strontium barium niobate (Sr_{1-x}Ba_xNb₂O₆, SBN) presents either a tetragonal or

an orthorhombic phase, depending on its composition as well as temperature. A

solid solution of SBN exists in the binary SrNb₂O₆ (SN) -BaNb₂O₆ (BN)

system. Investigations using X-ray diffraction suggest a morphotropic phase

boundary (MPB) around $x = 0.25$, which is characterized by the coexistence of

the tetragonal and orthorhombic phases. SBN with $x = 0.2$ presents a tetragonal

ferroelectric phase between 120 and 293°C, an orthorhombic phase below 120

°C and a tetragonal paraelectric phase above 293 °C.

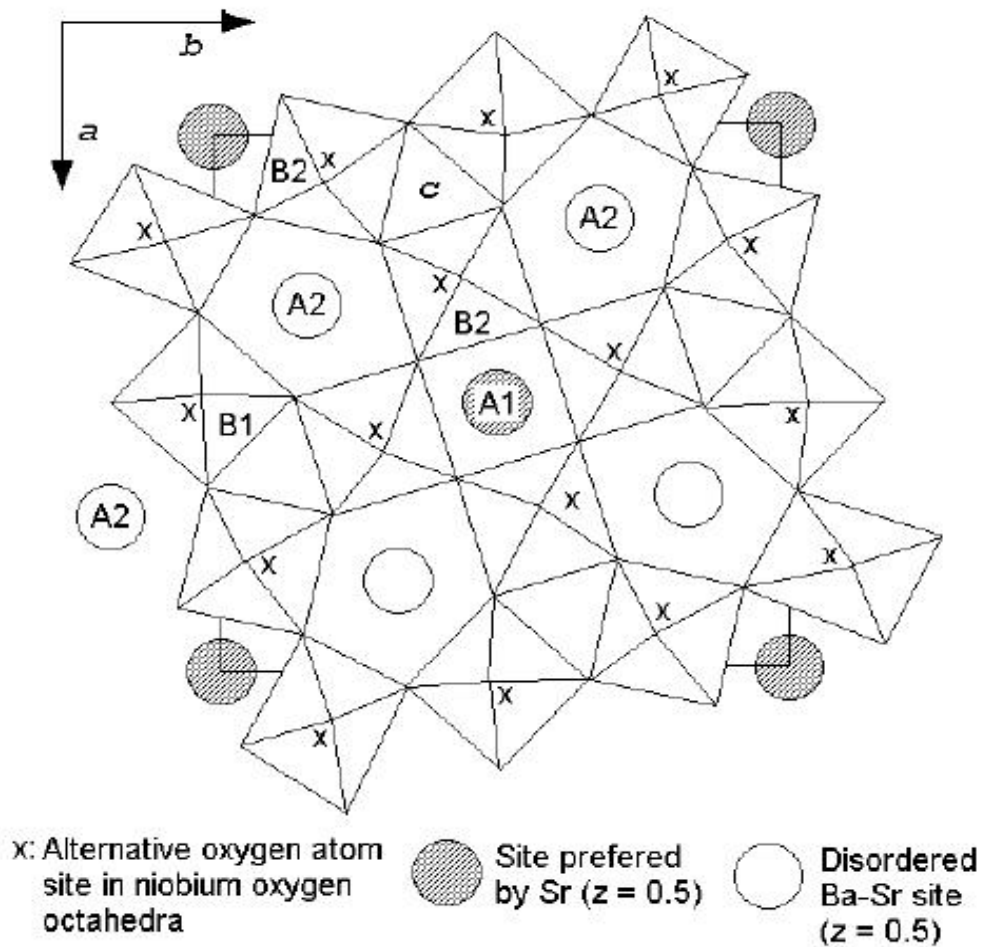


Figure 1.1 View of the SBN structure along the polar axis [*Jamieson et.al*]

The detailed structure of SBN has been reported by *Jamieson et al*, using X-ray diffraction. SBN ($0.25 < x < 0.75$) belongs to tetragonal tungsten bronze structure, with point group of $P4bm$. This structure consists of a framework of NbO_6 octahedra sharing corners which are occupied by oxygen. There are three types of interstitial site: i) Each of the $B1$ and $B2$ sites all possess distorted octahedra symmetry in this structure which is shown in the Figure 1.1. These sites are



fully occupied by niobium atoms; ii) The sites of $A1$ and $A2$ are occupied by either Sr ions or Ba ions, or both of them; iii) Also the third type are the metal ions which are substituted from the nearest mean plane of oxygen ions in the same sense, this sense defines the polar direction of the ferroelectrics. Above the ferroelectric phase transition the crystal is non-polar, and noncentrosymmetric. At this transition, the Sr ions, Ba ions and 20% of the Nb ions move into the oxygen planes, while the other 80% of the Nb ions are equally displaced above or below the oxygen planes. This implies that the internal energy of the crystal has a double minimum with respect to ionic displacement so that the transition is an order-disorder type.

The observation of optical birefringence and second harmonic generation of SBN well above the ferroelectric phase transition is consistent with this structure data. SBN has five formula units in each unit cell, that is, five Sr/Ba ions and six possible $A1$ and $A2$ sites. The structure shows that the distorted tetragonal $A1$ sites are occupied only by Sr ions (1.67 Sr ions for 2 $A1$ sites), while the distorted trigonal $A2$ sites are occupied by both Ba and Sr ions in a random manner (2.08 Sr, 1.25 Ba ions for 4 $A2$ sites). If the $A1$ site continues to be occupied only by Sr ions when the Sr/Ba ratio of the material changes, then



the entropy of distribution of the ions (the degree of randomness of the structure) becomes a minimum when $x=0.67$. At this point only Sr ions are in the $A1$ sites and Ba ions in the $A2$ sites. Today, this structure is still accepted for SBN.

Due to its special tetragonal tungsten bronze structure, SBN possesses many outstanding properties such as extremely high linear electro-optic ($r_{33} = 1340$ pm/V), nonlinear optical coefficient ($d_{33} = 12.8$ pm/V) and strong photorefractive effect. Indeed, SBN75 has the largest linear electro-optic coefficient of all the electro-optic crystals reported to date which is almost 50 times larger than that of LiNbO_3 , the most commonly used electro-optic material. The pyroelectric coefficient of bulk tetragonal SBN is also higher than those of other well known ferroelectric materials. Furthermore, to generate or amplify light, ferroelectrics are typically doped with rare-earth (RE) ions. With its incompletely filled tetragonal tungsten-bronze type structure, SBN can easily be doped with various RE or alkali ions to tailor and optimize certain properties for use in various devices. Up to now, SBN has been used in many optical devices such as pyroelectric infrared detector, phase-conjugated mirrors, electro-optic modulators, holographic storage, and photorefractive optics etc.



However, the growth of bulk SBN crystal has been proved to be difficult and expensive. [Thöny *et al.*] The heteroepitaxial or highly *c*-axis-oriented growth of SBN thin films of several micrometers thick is viewed as an alternative solution for electro-optic, photorefractive, and pyroelectric applications. For example, the desired SBN orientation for waveguide applications is with its optical axis (*c*-axis for SBN) orthogonal to the plane of the interface, so that the largest electro-optic and nonlinear optical coefficients can be accessed. In addition, to decrease the propagation optical loss, epitaxial SBN films with adequate surface smoothness are required. Therefore, technique to fabricate epitaxial thick SBN films is of paramount important to engineers and designers.

1.3 Pulsed Laser Deposition

By far, several kinds of fabrication techniques such as pulsed laser deposition (PLD), sol-gel, rf sputtering, metalorganic chemical vapor deposition, and liquid-phase epitaxy have been used. Among them, PLD has been shown to grow excellent epitaxial multicomponent oxide films.



1.3.1 History of Pulsed Laser Deposition

In the mid of 1960's, the ruby laser was used to vaporize and excite atoms from material surfaces by Breech and Cross. A few years later, deposition of thin films was obtained by ruby laser. This marked the very beginning of the development of PLD technique. With the use of the reliable electronic Q-switches lasers, a very short optical pulse with peak power density exceeding 10^8 W/cm^2 was available. In subsequent development of the laser technology, high efficiency harmonic generators were developed. They delivered powerful UV radiation. Due to short wavelength of the radiation, enhanced non-thermal interaction at the target surface was achieved. As a result, a quick and efficient congruent evaporation of target materials was made possible. Because of this, PLD process was shown to grow thin films with good stoichiometry easily. For the past thirty years or so, numerous reports have been published for the fabrication of crystalline films grown by PLD. Indeed, epitaxial semiconductor films, heterostructures, and superlattices produced by PLD have all been demonstrated. It has also been shown that the qualities of some of the PLD films are comparable to those grown by MBE. However, the most noted success of PLD is on fabrication of stoichiometric complex oxide thin films



such as superconducting $\text{YBa}_2\text{Cu}_3\text{O}_7$ or ferroelectric perovskites.

1.3.2 Mechanism of Pulsed Laser Deposition

The mechanisms involved in PLD are quite complicated. This is in direct contrast to the simplicity of the set-up itself. In essence high power laser energy is used as an external energy source to vaporize materials that subsequently deposit on substrates to form thin films. Usually a pulsed laser beam is focused onto the surface of a solid target. The strong absorption of the electromagnetic radiation by the solid surface leads to rapid evaporation of the target materials. The evaporated materials, named evaporants, consist of a mixture of different energetic species including atoms, molecules, electrons, ions, clusters, micro-sized solid particulates, and molten globules. A glowing plasma plume will be formed from the evaporants immediately in front of the target surface if the ablation is carried out in vacuum. Then the energetic species undergo thermal and non-thermal interaction with the substrate and ultimately lead to film formation and grain growth.



1.3.3 The Three Stages of Pulsed Laser Deposition Process

1.3.3.1 Laser-Target Interaction

When a high power laser beam is focused onto the target, all elements in the target surface are rapidly heated up to their evaporation temperature because of the high energy densities and short pulse duration. Due to local heating, temperature of order of 3500 °C is readily reached in a small volume near the target surface. As a result, materials are dissociated from the target, and then ablated out with stoichiometry as in the target. The ablation mechanisms involve many complex physical phenomena such as collision, thermal and electronic excitation, exfoliation and hydrodynamics.

1.3.3.2 Target to Substrate Gas Phase Transportation

The ablated materials are highly excited and resulted in a glowing plasma. The plasma plume possesses uniform translational energy of about 10-100 eV with small spread. Two types of particles, namely, the thermal induced particle and the non-thermal induced particle, will spread out as cosine and $(\cosine)^n$, where



$n \gg 1$, respectively. High ion to neutral atom ratio and many multiply ionized species are carried in the plasma as well.

1.3.3.3 Nucleation and Film Growth

The growth of thin films can be categorized into three conventional modes.

Three-dimensional island growth (Volmer-Weber) involves the formation of isolated islands on the surface. It only occurs when the cohesive energy of the atoms within the film is higher than that of the energy between the films and atoms on the surface. A very smooth epitaxial film is resulted in

two-dimensional full-mono-layer growth (Frank-van der Merwe) because of the higher cohesive energy between the films and the surface atoms than that of the film atoms. Mixed growth mode (Stranski-Krastanov) occurs for the interaction strength somewhere in the middle.



1.3.4 Advantage and Disadvantage of Pulsed Laser

Deposition

1.3.4.1 Advantage of Pulsed Laser Deposition

PLD offers several advantages for fabricating films. First of all, the fabricated films normally possess the same stoichiometry as the multicomponent targets. Secondly, the requirement of substrate temperature for fabricating crystalline films by PLD is usually lower than those utilizing other deposition methods such as thermal evaporation, electron-beam or ion-beam evaporation, d.c. or r.f. magnetron sputtering, chemical vapor deposition, and molecular beam epitaxy (MBE). Thirdly, because of the high energy density of the focused laser beam, the as-deposited energetic species have sufficient kinetic energy to migrate to their favorable site. Fourthly, in-situ growth of different materials is available by the PLD method. For example, using a rotating multi-target holder, the laser beam can be rastered different targets by setting a suitable alignment. As a result, in-situ growth of heterostructures is achieved by this way. The thin film can be deposited in any ambient gas by PLD as well. Finally, the start-up cost of PLD is low in comparison with, say, MBE.



1.3.4.2 Disadvantage of Pulsed Laser Deposition

There are three main disadvantages of using PLD. The deposition area is very small because of the limited angular spread of the plume. Deposited films of only about 1 cm^2 can be obtained in a typical PLD geometry. The uniformity of the film thickness cannot be maintained if the area of deposition is too large.

The maximum film thickness is obtained at the center of the plasma plume and decreases rapidly with the distance away from the center point. However, the uniformity can be modified by tilting and rotating the substrate as well as scanning of the laser beam. The second undesirable feature of PLD is that the as-deposited films are often covered with large particulates. The formation of the particulates is quite complicated. The particulates size can be as large as $\sim \mu\text{m}$, which is bigger than the thickness dimension of the deposited film. As a result, the degradation of the film properties occurs because of the presence of these large particulates on the film. This is particularly damaging in multi-layer systems. However, with the use of a blocking mask placed in between the substrate and the target holder during deposition, the particulate problem could be greatly reduced. Several approaches for reducing the number of particulates



such as dual laser beam, velocity filter, electromagnetic shutter etc are used as well. Finally, the target surface modification represents another disadvantage.

Repeated irradiation by high power laser causes pitting on the target surface. If unchecked, these target surface modifications can easily lead to reduced ablation yield and particulate formation.

1.4 Outline of Thesis

The essential background and the literature review of SBN are introduced in the first and second sections of this chapter, respectively. A brief introduction of PLD technique is described in the third section of this chapter. After that, the working principle of PLD, advantages and disadvantages of this method are discussed.

Chapter 2 reveals the basic background knowledge of optical waveguides. The definition, classification, development and applications of optical waveguides are also described in this chapter.

The experimental set-up of PLD system used in our studies is described in



chapter 3. Various characterization techniques such as X-ray diffraction (XRD), X-ray photoelectric spectroscopy (XPS), scanning electron microscopy (SEM), atomic force microscopy (AFM), optical transmittance and coupling prism technique are introduced. In the last section of this chapter, the experimental processes are briefly introduced. However, the detailed experimental conditions and parameters are given in the following chapters.

The investigation of bottom electrode material, which is an important component for waveguide application, is discussed in chapter 4. In the first section, the fabrication and structural characterization of lithium nickel oxide (LNO) targets are introduced. Afterwards, the fabrication of LNO films on (001) MgO substrates are discussed. The structural, optical properties and the conductivity of these LNO films are studied. Finally, the fabrication and characterization of SBN/LNO films deposited on MgO substrate using a two-step deposition process are discussed.

Chapter 5 describes the deposition of SBN films on MgO/TiN buffered silicon substrate. The structural and surface morphology properties of these heterostructures are presented. The waveguiding characterization is very



important for waveguide applications. The measurement of the waveguiding properties is discussed in the following section. The correlation between the structural and optical properties of these heterostructures is investigated.

The experimental results and important findings are discussed and concluded in the last chapter of this thesis. Suggestion for future investigation and development are given. The significance of this research is evaluated.



Chapter 2

Optical Waveguides

2.1 History of Optical Waveguides

Although dielectric guides have been studied by Hondros and Debye in 1910, the first interest in optical applications has only started in the late 1950's.

Several laboratories had developed the technology required to produce close-packed assemblies of glass fibers. Kapany and Burke originally approached the study of waveguide effects in fiber optics with a view to substantially eliminating them in devices designed for incoherent systems [Kapany N. S. and Burke J. J., 1961]. The achievement of lasing action in semiconductors by three groups in 1962 [Hall *et al.*, Nathan *et al.*, Quist *et al.*] was soon followed by the guidance in the p-n junction plane in 1963 [Yariv and Leite, Bond *et al.*] and the guiding action of a p-n junction was used in a modulator via the electric-optic effect in 1964 [Nelson and Reinhart]. The development of the p-n junction modulator has since followed that of the junction laser via the steps of epitaxial GaAs films [Hall *et al.*] and



heterostructures [Reinhart and Miller] in the early years of 1970's. The thin-film waveguide at optical frequencies is at least as old as the development of optical thin-film technology. We have been unable to determine when the thin-film guide was first studied. However, thin-film guides became candidates for potential communications applications until the late 1960's. Early work on thin films [Osterberg and Smith, 1964; D. B. Anderson, 1965] led eventually to the new concept of integrated optics [Miller, 1969]. The problem of coupling laser beams into planar guides was solved by the prism coupler [Tier *et al.*, 1969] and the grating coupler [Dakss *et al.*, 1970]. This technique appears to have very considerable advantages for integrated optics applications. The concept of integrated optical integrated circuits, that use an optical waveguide as a basic structure to implement compact and robust devices performing complicated functions for specific applications by integration of several elements, was introduced in the late 1960's. Since then, extensive research and development work has been performed in waveguide theory, waveguide materials and fabrication, and implementation of a number of passive, active, and functional devices. The waveguide devices developed thus far include optical couplers and filters, optical modulators, and switches based on electro-optic (EO) and acousto-optic (AO) effects, semiconductor laser



oscillators and amplifiers. Many sophisticated devices have also been developed by integration of waveguide components. They found many applications in optical communications, optical memories, and optical parallel signal processing and optical sensors. Although it took rather long time for them to be put into practical applications, recent progress has led to commercialization and great success, especially in the area of optical communications. Therefore, optical waveguides are one of the most important fundamental structures for device applications.

2.2 Waveguides Concepts

2.2.1 Total Internal Reflection

In recent year, optical waveguides have attracted much attention for their wide applications in communication systems. It has been known since long time ago that an optical wave can be confined in a narrow cross sectional region with a refractive index higher than that of the surrounding medium and guided through successive total internal reflections at the boundaries. The schematic diagram of total internal reflection is shown in Figure 2.1.

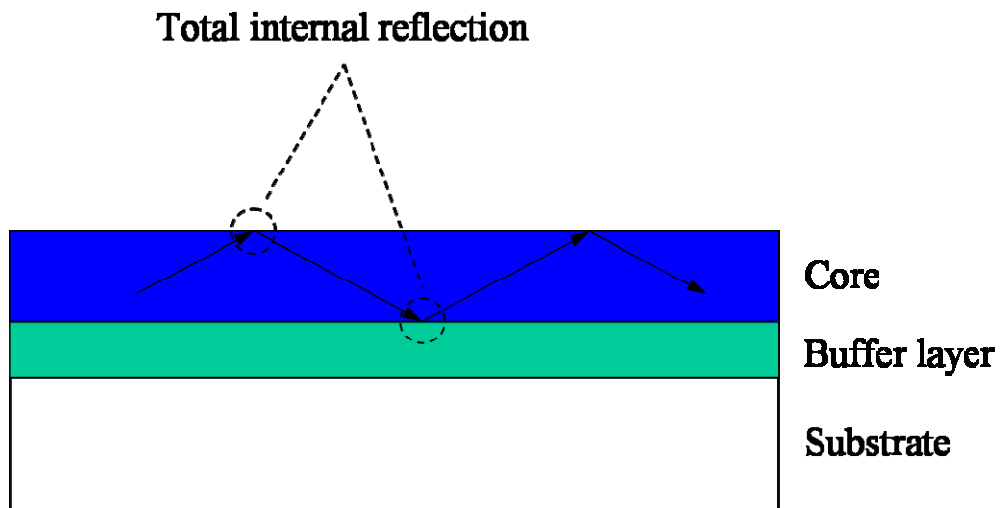


Figure 2.1 Schematic diagram of total internal reflection

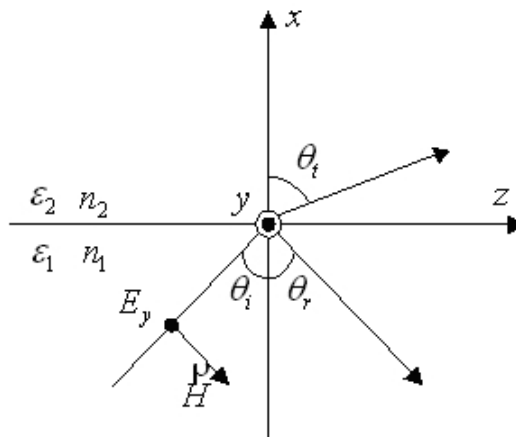


Figure 2.2 Schematic diagram of Snell's Law



Figure 2.2 is the schematic diagram of Snell's Law which described as below

$$\begin{aligned}n_1 \sin \theta_i &= n_1 \sin \theta_r = n_2 \sin \theta_t \\ \therefore \theta_i &= \theta_r \\ \sin \theta_i &= \frac{n_2}{n_1} \sin \theta_t\end{aligned}\tag{Eq. 2.1}$$

where θ_i , θ_r , θ_t are the angel of incident ray, reflected ray and transmitted ray, respectively.

When $\theta_t = 90^\circ$, from the Snell's law, we then have $n_1 \sin \theta_i = n_1 \sin \theta_c = n_2$,

$$\sin \theta_c = \frac{n_2}{n_1} \text{ or } \theta_c = \sin^{-1} \frac{n_2}{n_1} = \text{CriticalAngle}\tag{Eq. 2.2}$$

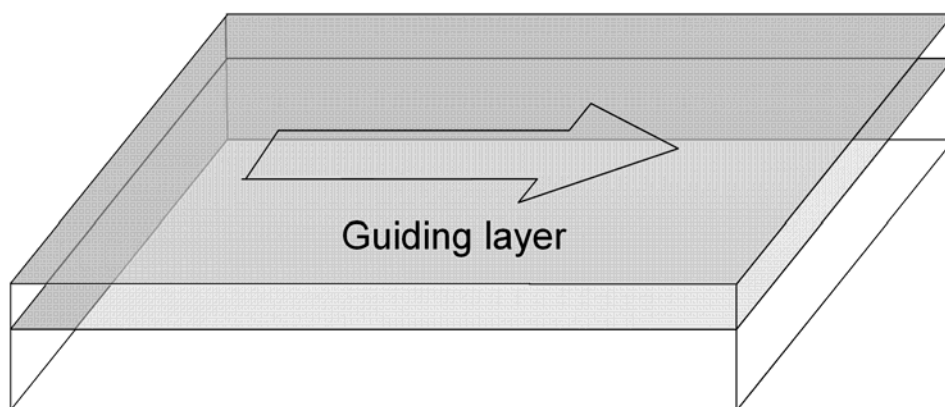
when $\theta_i > \theta_c$, the total internal reflection will be happened.

2.2.2 Slab and Channel Waveguides

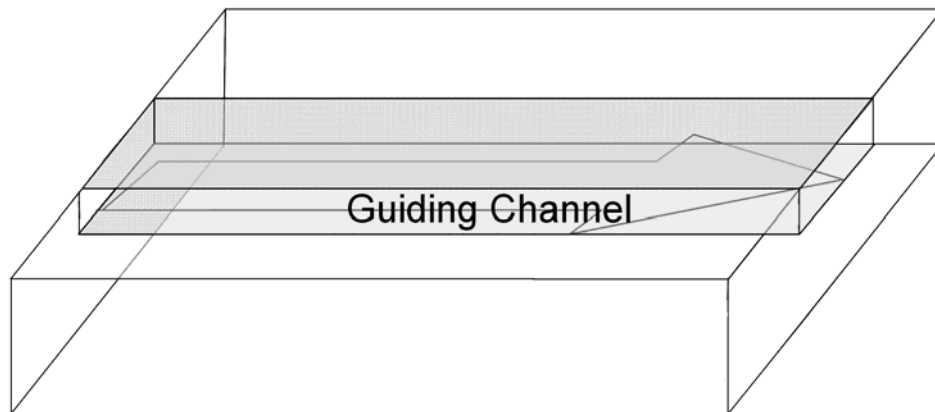
Optical waveguides are structure to confine and guide optical waves by the total internal reflection at dielectric interfaces. They are classified into slab



waveguides (planar waveguides) and channel waveguides. Slab waveguides, which provide two-dimensional confinement of an optical field in the guiding layer, as shown in Figure 2.3 (a), can easily be fabricated and are used as a simple model for analysis of NLO interactions. Channel waveguides, which provide three-dimensional confinement in the core region, as shown in Figure.2.3 (b), are much more suitable for implementation of NLO devices of high efficiency that require strong field confinement in a small cross-sectional area. In either case, it is required that the refractive index of the guiding (core) region be higher than that of the surrounding (cladding) regions. In ray optics, guiding wave can simply be interpreted in terms of the zigzag pass of a ray in a core with successive total internal reflections at the core/cladding interfaces, where the ray is incident at an angle larger than the critical angle.



(a) Slab waveguide



(b) Channel waveguide

Figure 2.3 Schematic illustrations of optical waveguides

2.3 Advantages of Optical Waveguides

One can expect several advantages offered by using the waveguide technologies in nonlinear optics (NLO). A channel waveguide of NLO materials can be used to confine optical waves in a small cross sectional area and maintain high optical intensity over a long propagation length without divergence by diffraction. This means that strong NLO interaction can be accomplished over a long interaction length, and therefore NLO devices that work at a high efficiency even with low or moderate input power. Compact



semiconductor lasers may be used as a pump source. Thus, the NLO instruments can evolve into miniaturized waveguide NLO devices, and this leads to drastic reduction in size, weight and power consumption.

Another important advantage is that the use of a waveguide offers new possibilities in phase matching; not only birefringent phase matching and quasi-phase matching using a periodic structure applicable to bulk NLO crystals but also mode-dispersion phase matching and Cerenkov-radiation-type phase matching can be employed in waveguide NLO devices. This may possibly lead to extension of the wavelength range or improvement in the efficiency.

Obviously, it is also possible to implement many sophisticated devices for advanced functions by integration of several waveguide NLO devices and/or integration of waveguide NLO components and peripheral waveguide components performing passive and active functions. Such integration would be essential for practical applications outside of laboratories.



Chapter 3

Experimental

All of the films were prepared by PLD technique using a Krypton fluoride (KrF) excimer laser with a radiation wavelength of 248 nm. The crystallinity of the target and the films were characterized by X-ray diffractometry (XRD) with Cu K_{α} radiation. The Li concentration in the LNO thin films was determined by X-ray photoelectron spectroscopy (XPS). The surface morphology and cross-section of the films were studied by scanning electron microscope (SEM). The surface roughness was measured by atomic force microscope (AFM). Finally, the optical transmittance and waveguide properties were determined by an UV-visible spectroscopic system and a prism coupler, respectively.

3.1 Sample Fabrication

3.1.1 Pulsed Laser Deposition

A standard PLD experimental set-up generally includes three main parts, namely,



the laser, the optics and the vacuum deposition chamber. A schematic diagram of the set-up is shown in Figure 3.1. Basically, excimer is formed in a gaseous mixture of the component gasses such as Kr, F₂, He and Ne. The ionic and electronically excited species are created by the avalanche electric discharge excitation (~ 40 kV). The excited species react chemically to produce the excimer molecules, of which the ground state is repulsive and tends to dissociate rapidly. In this study, a Lambda Physik COMPex 200 KrF excimer laser was used. The output spatial profile of this particular laser was a “top hat” with a rectangular dimension of $1 \times 3 \text{ cm}^2$. The laser could be operated at a maximum repetition rate of 20 Hz, while the maximum laser energy per pulse could be up to ~ 600 mJ. As the incident photon has a short wavelength (248 nm in our PLD system), the interaction between the oxide target and the laser is dominated by non-thermal interactions rather than by thermal process. As a result, no or very little melting is taken place on the target surface. One of the advantages offered by PLD technique is its flexibility. With the use of the beam steering mirrors, a single laser could serve a number of deposition chambers.

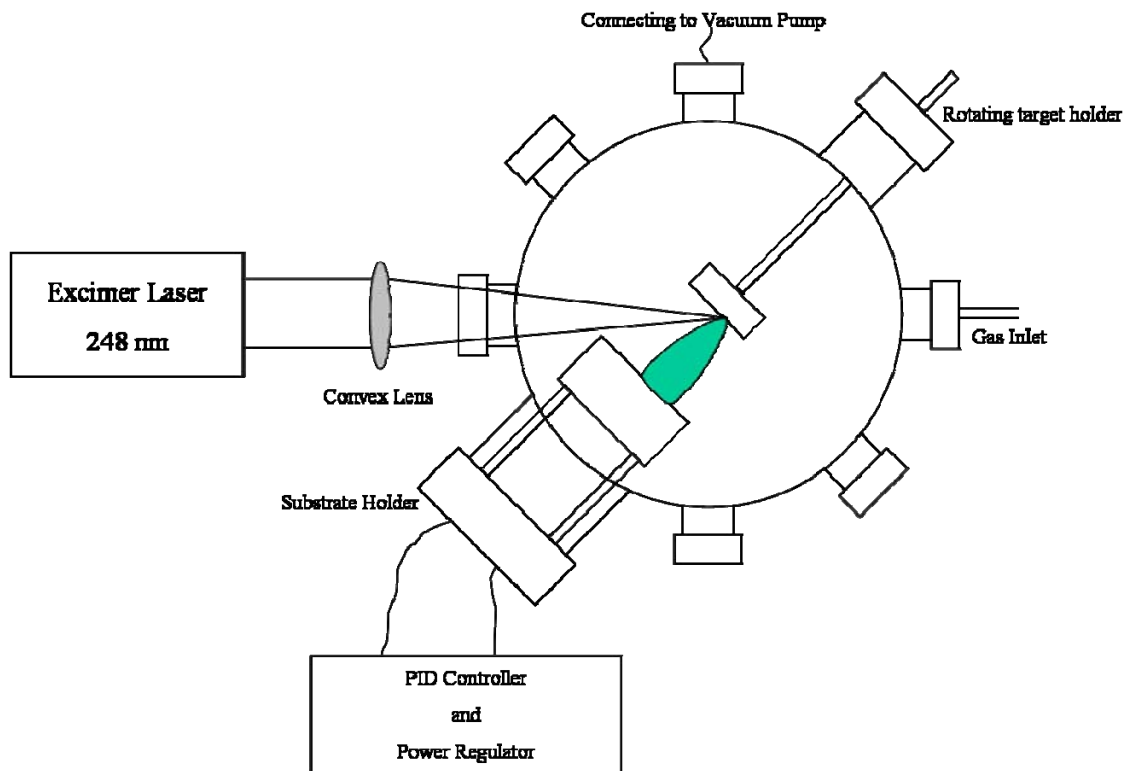


Figure 3.1 Schematic diagram of PLD experimental set-up

For coupling of the laser to the target we need to use lenses, apertures, mirrors and laser windows in our deposition system. Instead of ordinary glass optics, UV-grade fused silica lenses and window were used because of the expected good laser transmittance. UV-grade fused silica can transmit over 90% of the 248 nm radiation. To achieve the target ablation, laser fluence of several J/cm^2 was required. The lens with focal length about 30 cm was equipped in our PLD



set-up. The function of the lens is to collect the radiation from the excimer laser source and focus them on to a small spot on the target surface. Therefore, the focused laser spot was converged through the chamber window onto the surface of the target.

In Figure 3.1, the vacuum chamber was connected to a rotary pump (ALCATEL CIT 2021). All the oxide thin films produced in this research were deposited in a chamber which was evacuated by a rotary pump to vacuum of no better than 10 mTorr. The pressure of the chamber was monitored by a manometer (MKS PDR-D-2) in the range from 10 to 10^{-3} Torr. However, for some cases such as growth of TiN and MgO films, the growth process may require a higher vacuum condition. In these cases, an additional diffusion pump (ALCATEL PAD CRYSTAL 102) was used to evacuate the chamber to a base pressure of about 10^{-6} Torr while an ionization vacuum gauge (ULVAC G1-TL3) was employed to monitor the pressure.

The substrate holder was equipped with a heating filament that could be heated up to 750 °C. Total resistance of the filament was smaller than 14 Ω . The heating process was controlled by a PID (SHIMADEN SR-18) and a power



regulator (PAC25-0321). A K-type (Nickel-Chromium, Nickel-Aluminium) stainless steel shielded thermocouple was employed for monitoring the temperature. The substrates were then secured to a stainless steel resistive heater using silver paste to get a good thermal contact between the substrate and the heater.

In general, oxygen environment was needed for growing oxygen stoichiometric thin films. So, a gas inlet port was used to introduce of oxygen gas of 99.7% purity into the chamber to a desired oxygen pressure for film growth.

3.1.2 Target Fabrication

All the pulsed laser ablation targets were fabricated by a standard solid state reaction method. The powders were mixed with ethanol according to the desired stoichiometric ratio and then ball milled for 12 hours. The mixture was calcined to drive away the organic components from the mixed powder and to allow the chemical reaction occur. The calcinated product was then re-milled again into powder in a mortar and pressed by an oil-compressor at a certain pressure into circular pellets about several mm thick. Each of the calcination



and sintering processes were done in air and lasted for at least 10 hours at the optimal temperature. The detailed preparation parameters of LNO and SBN targets will be given in the following chapter.

3.1.3 Substrate Preparation

In this study, single crystal MgO and single crystal Si were selected to be the substrates for our studies. All the substrates were purchased from commercial vendors, with the same dimension of 10mm (length) \times 5mm (width) \times 0.5mm (thickness). In order to remove the grease due to the contamination on the surface, which will greatly affect the quality of the as-prepared film, the substrate must be thoroughly cleaned before it can be used. We cleansed and degreased the substrates ultrasonically for 10 minutes using spectroscopic grade acetone. In order to remove the native oxide layer, the Si substrates were etched by a 10% HF solution for 15 min before ultrasonical cleaning,

3.1.4 Deposition Process

Before the deposition, proper alignment of the target, substrate and optics was



made. The target was mounted on a rotating target holder. The target-substrate distance was kept at 35 ~ 45 mm. Before the actual ablation process the mirrors and the lens were firstly and finely aligned, so that the laser beam passed the window of the chamber and focused onto the target surface. The chamber was then continuously evacuated by a rotary pump until the pressure was below 10mTorr. After that, oxygen was filled into the chamber to the desired deposition pressure, such as 100 mTorr. A final check of the beam alignment was achieved by observing the laser induced plasma plume. Two important points should be carefully attended to. The first is that the plume should emanate from the target at a direction normal to the target surface, while the other is that the tip of the plume should point toward the centre of the substrate holder.

After these delicate alignment processes had been carefully completed, the chamber was re-filled back to atmospheric pressure. The substrate was secured to a stainless steel resistive heater/substrate holder using silver paste. The reason for using silver paste in the adhesion is that it acts as the heat conduction medium in between the substrate and the heater. In order to find out the thickness of the film, a small strip of stainless steel was placed at the corner of



the substrate surface. As a result, the thickness of the film could be determined by introducing a step on the film. Then the chamber was evacuated by a rotary pump to 10 mTorr again. The ohmic heater was turned on and waited until reaching the desired deposition temperature. Then, oxygen was filled into the chamber to 100 mTorr. When all the parameters for film deposition were stable, the laser was pulsed at a repetition rate of 10 Hz with an on-target laser fluence of 3 J/cm^2 . The deposition time was lasted for 10 minutes to obtain films of ~200 nm thick. Finally, post annealing was carried out at the same deposition temperature for 10~15 minutes, so that better crystalline films were obtained. The detailed conditions of deposition of the LNO, TiN, MgO and SBN films will be presented in chapter 4 and chapter 5.

3.2 Characterization Instruments

3.2.1 X-ray Diffraction (XRD)

Although optical microscopy was an invaluable tool in the early days of crystallography, the information that it revealed was rather limited.

Measurement of the angles between the faces of well defined naturally



occurring mineral crystals enabled the overall symmetry of the crystal structure to be inferred. However, the large wavelength of visible radiation meant that the resolution obtainable was much too poor to resolve detail on an atomic scale, and no information as to the size of the unit cell and the actual positions of the atoms could be deduced. X-rays discovered in 1895 are electromagnetic waves like visible light but with a much smaller wavelength. The wavelength of X-ray is typically about 10^{-10} m and is of the same order of magnitude as the interatomic spacings in crystals, and so the network of atoms in solids acts like a naturally occurring three-dimensional diffraction grating.

X-ray diffractometry (XRD) is a common and non-destructive method for characterization of crystal structure and for determination of atom location of various materials in bulk solids, powders, or thin films. It has been extensively used to investigate the structural qualities of thin films. Figure 3.2 shows a schematic diagram of the X-ray diffraction of a crystal. When X-rays from the X-ray source interact with the film, absorption and reflection from the crystal planes will occur. The atoms in the crystal become diffraction centers. As a result, constructive interference in certain direction will be produced.



If the diffraction follows the Bragg's Law, the reflected beam will possess maximum intensity.

$$n\lambda = 2d\sin\theta \quad (\text{Eq. 3.1})$$

where n is the order of the intensity maximum, λ is the X-ray wavelength, d is the interplanar spacing and θ is the angle of incident of X-ray beam.

The value of interplanar spacing d in simple cubic structure can be calculated as

$$d = \frac{a}{\sqrt{h^2 + k^2 + l^2}} \quad (\text{Eq. 3.2})$$

where h , k , and l are the Miller index and a is the lattice constant of crystal structure.

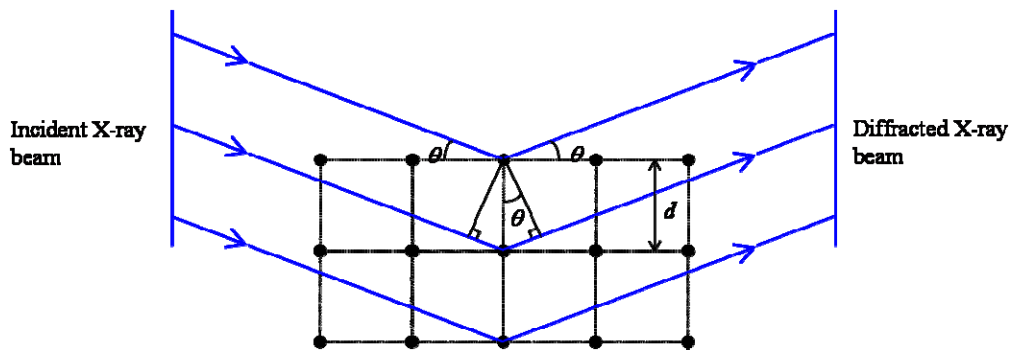


Figure 3.2 Schematic diagram of the X-ray diffraction of a crystal

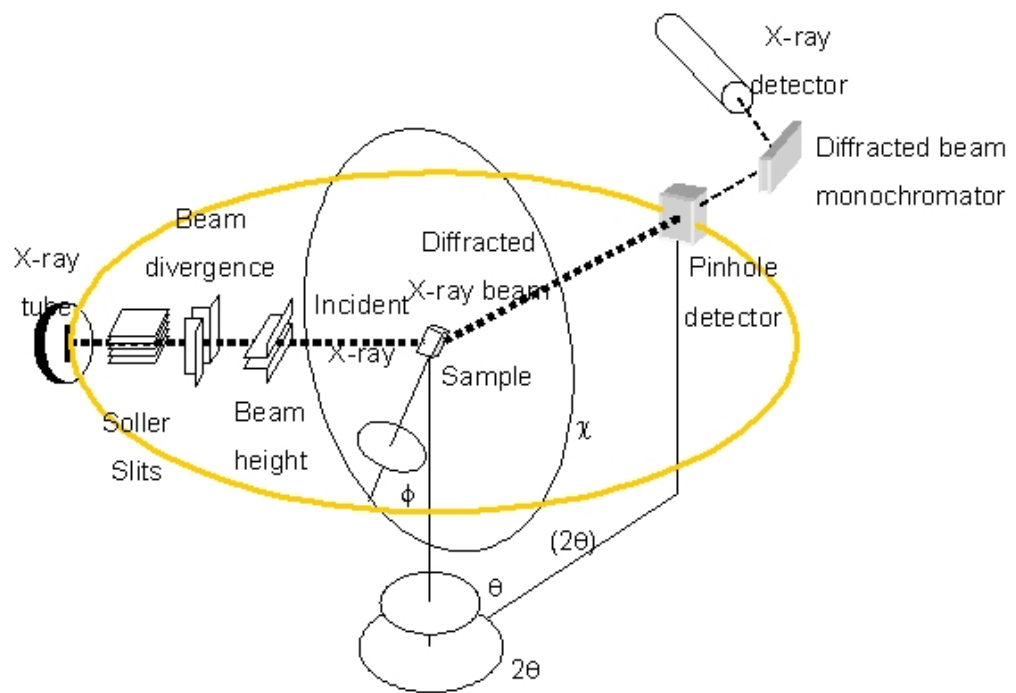


Figure 3.3 Schematic diagram of a typical XRD system



The structural properties of the thin films were characterized by X-ray diffractometer (Philip, X'pert system). Cu K_{α} radiation with wavelength of 1.54 Å was used and the unwanted Cu K_{β} radiation was filtered off by a Ni filter. Figure 3.3 shows the X-ray source, different kinds of slits, monochromator and detector. Also, there are four rotating axes, namely, θ (ω), 2θ , χ , and ϕ for different scan modes. In this project, θ - 2θ scan, ω scan and ϕ scan were performed in order to investigate the crystalline structure and the epitaxial quality of all the deposited thin films. The crystalline phases of the films and crystalline orientations paralleled to the substrate surface were determined by the θ - 2θ scan while the ω scan provided quantitative measurements of the film's orientations. The ϕ scan was used to determine the epitaxial growth relationship between the single crystal film and substrate.

In the θ - 2θ scan, the X-ray tube is fixed at certain position. When the sample rotates a certain angle with respect to the X-ray beam axis, the detector rotates twice of that angle, such that, the detector follows the reflected ray and receives the strongest signal from the diffraction. The patterns we got reveal the crystal structure of the film according to the database. From the data calculation, we can obtain the information of crystal phases, such as lattice constants and



orientations. However, only one set of planes of a family ($h00$) should be observed if films are epitaxially grown. So, we do not know whether the films are epitaxially grown on the substrate or not even if one set of planes from a single family of peaks. We can only conclude that the films are highly oriented in that direction.

On the other hand, ω scan (rocking curve) mode could help to retrieve the information of in-plane orientation. The X-ray source and detector are fixed at certain θ angle for a special orientation of crystal plane. The sample is scanned (rocked) about ω axis for a few degrees and then a broad profile will be obtained. Films having better aligned grains give narrow diffraction peaks. The value of the Full-Width-at-Half-Maximum (FWHM) of the rocking curve used to determine the growth quality of the film. The smaller the value of FWHM, the better is the grain orientation. Generally, if it is less than or around 1° , a highly oriented film is considered.

In fact, θ - 2θ scan and ω scan only provide limited information and are not adequate to give the quality of the highly epitaxial film and the substrate. In order to characterize the in-plane crystalline feature of the film, ϕ scan is



required. First of all, the ϕ angle is tilted to 45° along the χ axis for simple cubic structures, the 2θ and θ angles are fixed at the diffraction peaks of a selected plane such as (100) . Then a 360° ϕ scan is performed to investigate the peaks appeared and identify its four-fold symmetric. If the two sets of peaks from the film and substrate are aligned at the same angles and separated by 90° which corresponding to (101) , $(\bar{1}0\bar{1})$, $(10\bar{1})$ and $(\bar{1}01)$, it is concluded that the film is cube-on-cube epitaxially grown on the substrate. For tetragonal structure, it also shows four-fold symmetry with different tilting angle of χ axis, which depended on the ratio of the longer lattice constant against the shorter ones as well as the growth direction.

3.2.2 X-ray Photoelectron Spectroscopy (XPS)

X-ray photoelectron spectroscopy, also known as electron spectroscopy for chemical analysis (ESCA), is probably the most widely used surface analysis technique based on the photoelectric effect. When a beam of X-rays is directed onto a sample, the interaction between the X-ray photon and the core level electron of an atom causes a complete transfer of the photon energy to the electron. The electron then has enough energy to escape from the surface of the



sample. This electron is referred to as the photoelectron. The basic principle of XPS is schematically shown in Figure 3.4. For an electrically conductive solid, the binding energy of the core level electron (E_b) can be calculated using the following equation.

$$E_b = h\nu - E_k - \phi \quad (\text{Eq. 3.3})$$

where $h\nu$ is the incident X-ray photon energy, E_k is the kinetic energy of the photoelectron and ϕ is the work function of the spectrometer which is about 4-5 eV. The photon energy is known from the X-ray source employed (1486.6 eV for Al $K\alpha$ and 1253.6 eV for Mg $K\alpha$, the two most commonly used sources) and E_k can be measured by the XPS spectrometer. For insulating materials such as polymers, however, surface charging has to be considered and equation mentioned above should be rewritten as

$$E_b = h\nu - E_k - \phi - C \quad (\text{Eq. 3.4})$$

where C is a constant which is unknown and varies from sample to sample.

Therefore, for insulating materials, the electron binding energy is usually

determined by using an internal reference peak.

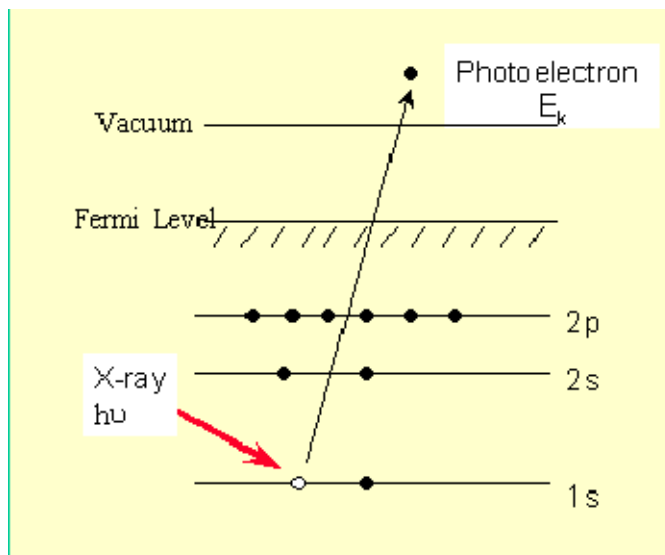


Figure 3.4 Schematic diagram of the basic principle of XPS

Elements have unique electron binding energies. Therefore, knowing the electron binding energy allows the identification of various elements. XPS is thus able to detect all elements except hydrogen. Furthermore, the electron binding energy is also sensitive to the electronic environment of the atom. When an atom is bonded to another atom of an element having a different electronegativity, the electron binding energy may increase or decrease. This change in binding energy is called the chemical shift, which can be used to provide chemical information of a molecule or compound.



Although X-rays penetrate deeply into the sample, the photoelectrons can only escape from a region near the surface. The sampling depth of XPS is given by the following equation.

$$d = 3\lambda \sin \theta \quad (\text{Eq. 3.5})$$

where λ is the attenuation length of the photoelectron and θ (take-off angle) is the angle between the sample surface and the analyser. By changing the take-off angle, the chemical information at various depths of the near surface region (from 10 to 100 Å) can be obtained (non-destructive depth profiling). In conjunction with ion beam sputtering, composition at deeper depths can also be obtained (depth profiling).

XPS is also a quantitative technique. The XPS peak intensities after normalized by the sensitivity factors can be used to calculate the surface chemical composition by using the following equation



$$C_i = \frac{I_i/S_i}{\sum_i^m I_i/S_i} \quad (\text{Eq. 3.6})$$

where C_i is the concentration of an element i , m is the number of elements in the sample, I_i and S_i are the peak area and the sensitivity factor of the element i , respectively.

In this project, a physical electronics 5600 multi-technique system (ULVAC-PHI 5600) was used to determine the Li concentration of the LNO thin films.

3.2.3 Scanning Electron Microscopy (SEM)

The surface morphology and cross-section of the deposited films were observed by a scanning electron microscope (Leica Stereoscan 440). Information such as surface morphology of the film, problems associated with particulates from the plane view of SEM micrographs, interface quality and the film thickness from the cross-section view could be obtained.



The working principle of SEM is that a high energy and tightly focused electron beam is scanned across the specimen surface. The electrons can undergo several interactions with the specimen. The interactions can be classified into two types, elastic or inelastic events. As a result, a variety of signals such as secondary electrons, backscattered electrons and characteristic X-rays are generated. Each of them can be used to characterize a material with respect to specific properties. It is because the collected signals vary with the changes in composition, texture or topography at the specimen surface.

Not all the specimen can be analyzed by SEM directly. For example, analyzing non-conducting materials is difficult. Negative charges will be built up gradually from the bombardment by the high energy electron beam. Thus, an abnormal contrast and splitting of the image result from the uneven distribution of the negative charges on the sample. To avoid this charge accumulation, a very thin (10-20 nm thick) coating of gold layer is normally placed on the surface of the sample.



3.2.4 Atomic-Force Microscopy (AFM)

An atomic force microscope (Burleigh, Metris-2000) was used to characterize the surface morphology of our thin films especially in the determination of lateral grain size and the surface roughness of the films. The AFM invented in 1985 was developed to overcome a basic drawback with STM that it could only image conducting or semiconducting surfaces. The AFM, however, has the advantage of imaging almost any type of surface, including polymers, ceramics, composites, glass, and biological samples.

Most AFM systems use a laser beam deflection system where a laser is reflected from the back of the flexible cantilever and onto a position-sensitive detector. By detecting the difference in the photodiode detector's output voltages, changes in the cantilever deflection or oscillation amplitude are determined. AFM tips and cantilevers are microfabricated from Si or Si₃N₄. Typical tip radius is from a few to 10s of nm. The scanning motion is conducted by a piezoelectric scanner which scans the tip in a raster pattern with respect to the sample (or scans the sample with respect to the tip).

Because the AFM relies on the forces between the tip and sample, knowing these forces is important for proper imaging. The force is not measured directly, but calculated by measuring the deflection of the cantilever, and knowing the stiffness of the cantilever. Hook's law gives

$$F = -kz \quad (\text{Eq. 3.7})$$

where F is the force, k is the stiffness of the cantilever, and z is the bent distance of the cantilever. Figure 3.5 shows the interaction force between tip and sample as a function of distance between them.

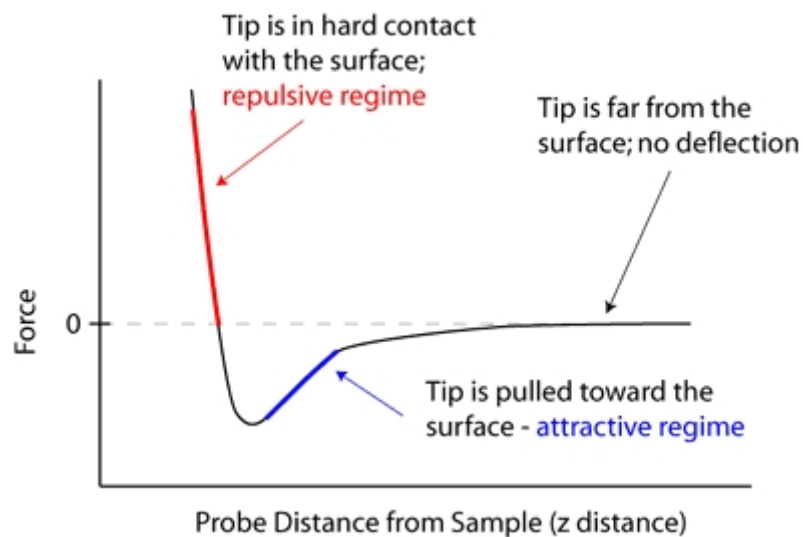


Figure 3.5 Interaction force between tip and sample as a function of distance



The AFM also can be operated in different imaging modes. They are the contact mode, noncontact mode and tapping mode. Scan area of $0.5 \times 0.5 \mu\text{m}^2$ in contact mode was used in our studies.

3.2.5 UV-Visible Spectrophotometer

Optical transmittance of the transparent films was measured by an UV-visible spectroscopy system (Agilent 8453). The sample compartment of the Agilent 8453 spectrophotometer is opened. Unlike conventional instruments the Agilent 8453 does not suffer from ambient false light. The open sample area makes it easier to access it generally and to connect tubing to a flow cell or thermostatable cell holder. Because spectrophotometer is a single beam instrument so we must have a blank measurement before measuring the samples. For high accuracy measurements, the blank and the sample measurement should closely follow each other. In our study, firstly, we put nothing on the sample holder to measure the transmittance in the air as reference. Then, measured the transmittance of MgO substrate and saved the result as a new baseline. Subsequent measuring of sample provided the optical

transmittance of the deposited films. Figure 3.6 shows the set-up of spectrometer for transmission measurement.

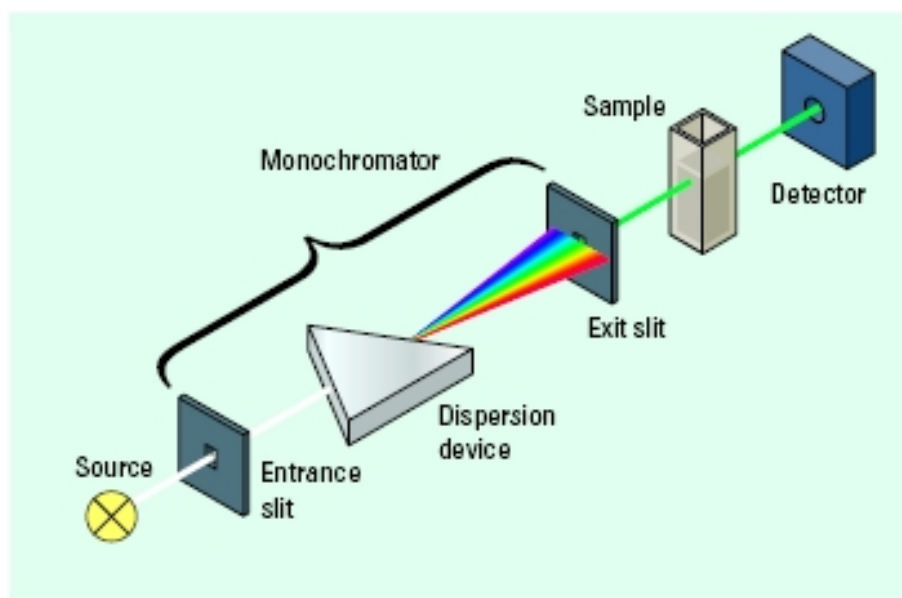


Figure 3.6 Schematic diagram of spectrometer set-up for transmission measurement

When light passes through or is reflected from a sample, the amount of light absorbed is the difference between the incident radiation (I_0) and the transmitted radiation (I). The amount of light absorbed is expressed as either transmittance or absorbance. Transmittance usually is given in terms of a fraction of 1 or as a percentage and is defined as follows:



$$T = \frac{I}{I_o} \quad \text{or} \quad \%T = \frac{I}{I_o} \times 100 \quad (\text{Eq. 3.8})$$

Absorbance is defined as follows:

$$A = -\log T \quad (\text{Eq. 3.9})$$

For most applications, absorbance values are used since the relationship between absorbance and both concentration and path length normally is linear.

3.2.6 Prism Coupler

Thin films are generally used as a planar light guides in various integrated optic devices. The main parameters characterized are the refractive index n and the film thickness h . In many determination methods, one method that is particularly well adapted to this problem is the prism coupling technique. It is simply and quickly gives accurate results. A schematic diagram of the experimental setup (Metricon 2010, USA) of TM mode measurement is shown in Figure. 3.7. In the prism-film coupling method, at certain discrete incident

angles, called mode angles, photons can tunnel across the air gap to form an optical propagation waveguide mode, causing a sharp drop in the intensity of light reaching the detector. This corresponds the drop peaks in the profile that we have obtained. The measured n_{TE} and n_{TM} thus represent the ordinary refractive index n_o and the extraordinary refractive index n_e of the films, respectively.

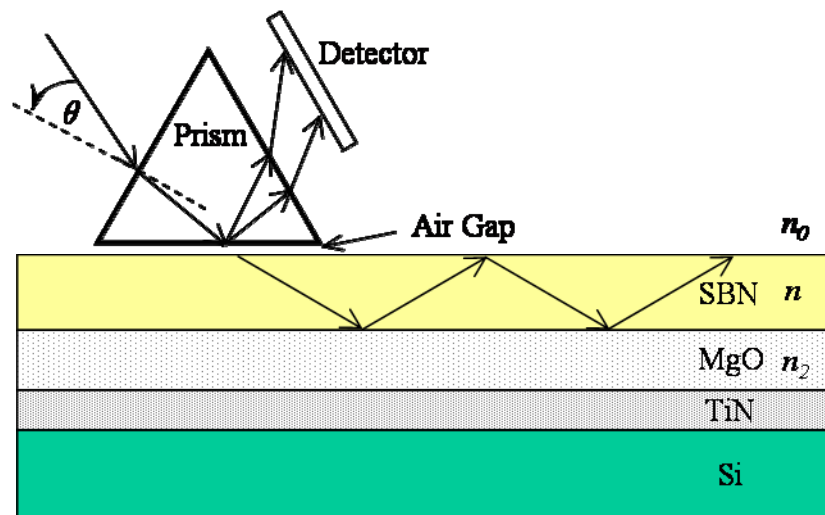


Figure 3.7 Schematic diagram of the experimental setup of TM waveguide mode measurement

Following Ulrich and Torge, the refractive index and thickness of waveguide films can be calculated using the following equation.



$$\begin{aligned} N_m &= \sin \alpha_m \cos \varepsilon + (n_p^2 - \sin^2 \alpha_m)^{1/2} \sin \varepsilon \\ 2\pi h(n^2 - N_m^2)^{1/2} / \lambda &= m\pi + \phi_0(n, N_m) + \phi_2(n, N_m) \quad (\text{Eq. 3.10}) \\ \phi_i(n, N_m) &= \tan^{-1} \left[\left(\frac{n}{n_i} \right)^{2\rho} \left(\frac{N_m^2 - n_i^2}{n^2 - N_m^2} \right)^{1/2} \right] \end{aligned}$$

where m represents the m th mode, $\rho=0$ for TE modes and $\rho=1$ for TM modes. $i=0, 2$. λ is the wavelength of the laser. n_p is the refractive index of the prism. α_m is the coupling mode angle of the m th mode. ε is a constant of 44.98° , determined by the type of the prism. h is the thickness of the waveguide layer. n_0 , n , and n_2 are refractive indices of the air gap, the waveguide layer, and the cladding layer, respectively. Based on the measured TE and TM modes at 632.8 nm, the refractive indices n_o and the n_e of films are determined. Also, the thickness of the waveguiding layer can be calculated from the measured data if two or more peaks of each mode appear in the profile.

Comparing with other methods, coupling prism has two important advantages:

- (i) it requires only the measurement of angles, which can be done conveniently and with high precision.
- (ii) If the film is thick enough to allow the observation



of more than two modes of the same polarization, the method becomes a self-consistent one because the two unknowns n and T are then determined from more than two independent measurements. This improves the accuracy and greatly increases the confidence in the results.

However, there are also some disadvantages to this method that limit its applicability: (i) the film must be thick enough to permit the propagation of at least two modes. If only one mode can be observed, we may still use the prism coupler to determine one of the parameters n and T if the other is known from an independent measurement. (ii) For reasons of convenient observation, a monochromatic laser beam should be available as the light source at the wavelength at which n is to be determined. (iii) Because it is usually necessary to press the film mechanically against the base of the prism, the method does not work contactless. Yet, if care is taken, the measurement is not destructive, either. In this respect, the method is obviously suited better for hard films than for soft films. (iv) Finding the coupling angles requires a certain degree of skill and experience. Difficulties may occur due to excessive losses in the films, causing a broadening of the modes beyond recognition. Typically, absorption up to 20 cm^{-1} in the direction of propagation is tolerable, although it will



already reduce somewhat the accuracy of the measurement. (v) The evaluation of the measurements requires lengthy, although simple, calculations. Therefore, the method is practical only where a programmable computer is available.



Chapter 4

Fabrication and Characterization of LNO and SBN/LNO Films Deposited on (001) MgO Single Crystal Substrates

4.1 Introduction

Ferroelectric $\text{Sr}_{1-x}\text{Ba}_x\text{Nb}_2\text{O}_6$ ($0.25 < x < 0.75$, SBN) with tetragonal tungsten bronze (TTB) structure has attracted great interest because of their excellent optical properties, such as extremely high electro-optic coefficient ($\gamma_{33} = 1340 \text{ pm/V}$) and large nonlinear optical coefficient ($d_{33} = 12.8 \text{ pm/V}$). Furthermore, SBN thin films have received extra attentions due to their potential applications over many areas. Recently, SBN waveguides have widely been studied because they provide the compatibility of integration with optical systems and other miniaturized devices. These optical waveguides can be obtained by depositing SBN films on a substrate of lower refractive index such as MgO substrate. Apart from the SBN guiding layer, the transparent conductive oxide (TCO) film underlying the guiding layer which acts as the



bottom electrode is also required in the waveguide structure.

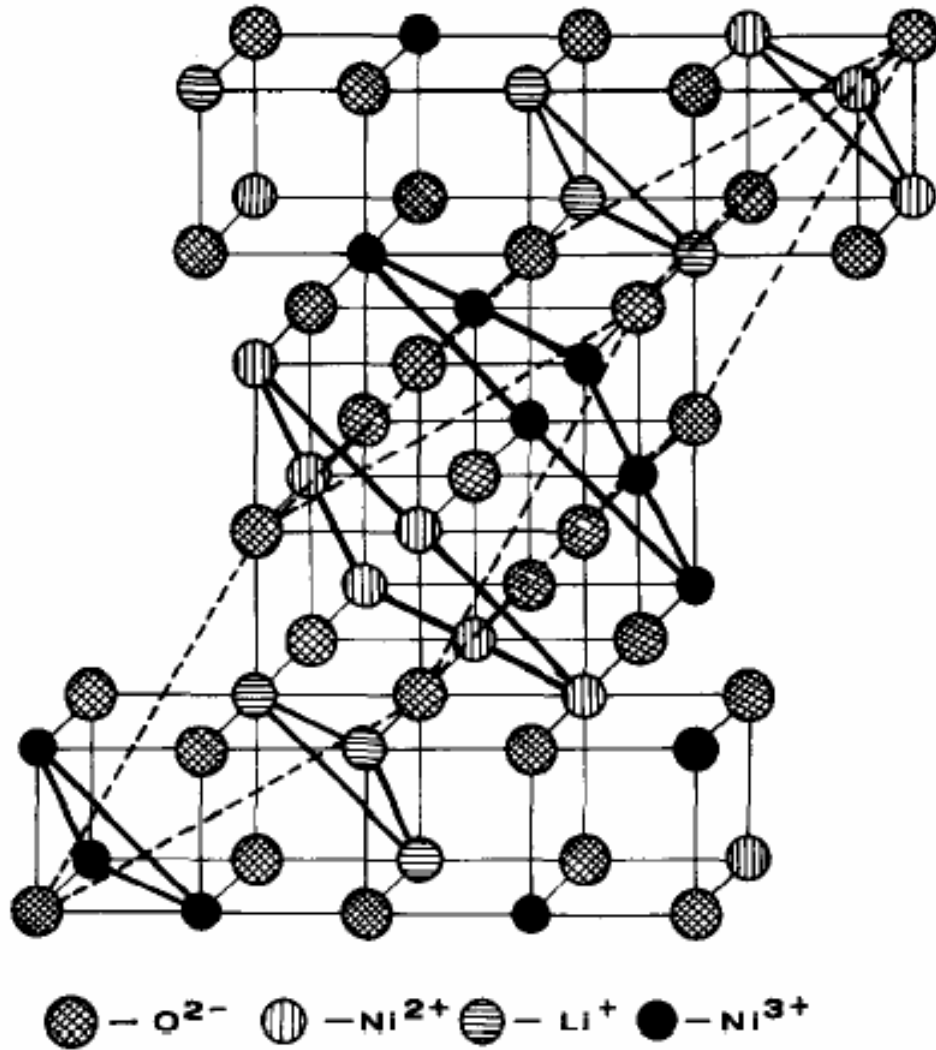


Figure 4.1 Schematic representation of $Li_xNi_{1-x}O$ ($x \approx 0.3$) structure



Among different conductive transparent films, lithium nickel oxide ($\text{Li}_x\text{Ni}_{1-x}\text{O}$, LNO) thin film has high electrical conductivity and good optical transmittance. It has cubic structure with a lattice constant of 0.414 nm and structurally matches with both the MgO and SBN layer. Therefore, in our project, LNO was selected as both a bottom electrode and buffer layer in our waveguide structure. Early studies showed that the crystallographic structure of LNO changes with lithium contents in the Li-Ni-O solid solutions. For low lithium contents ($x < 0.31$), LNO has a cubic NiO-like (NaCl-type) structure and is generally presented as $\text{Li}_x\text{Ni}_{1-x}\text{O}$; for $x > 0.31$, LNO changes to hexagonal structure due to the ordering of cations in alternating layers within the oxide lattice. The solid solution is usually characterized as $\text{Li}_{2x}\text{Ni}_{2-2x}\text{O}_2$ to point out the structural difference. Figure 4.1 shows the schematic representation of the $\text{Li}_x\text{Ni}_{1-x}\text{O}$ ($x \approx 0.3$) structure. It is generally formed by ordering of part of Ni^{2+} and Ni^{3+} in neighbor (111) planes, while the common subunit structure is a “sandwich”-type cluster formed by ordering of part of the Li^+ , Ni^{2+} and Ni^{3+} ions in alternating (111) cubic planes. Only the cubic-structure LNO can be grown with a desired epitaxial structure when we deposit the films. So, in our studies, in order to find the optimum lithium content, a series of $\text{Li}_x\text{Ni}_{1-x}\text{O}$ films with different lithium content ($x = 0.15, 0.2, 0.25, 0.3, 0.4, 0.5, 0.6$) were

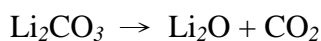


deposited on MgO. Here x represents the initial lithium content used in the target fabrication. Lithium contents larger than $x = 0.31$ were used because lithium ions evaporate easily during the sintering and deposition process. After the deposition of the LNO layer, the effects of the lithium content on the structural and optical properties as well as the conductivity of the LNO and SBN films were investigated.

4.2 Fabrication and Characterization of LNO Targets

4.2.1 LNO Targets Preparation

Both the LNO and SBN targets were prepared by conventional solid state reaction. Following the method of Pickering *et al.*, raw materials of AR grade Li_2CO_3 and NiO powders were used to fabricate the LNO targets. The formation of the solid solution from NiO and Li_2CO_3 powders mixture takes place as in the following reactions:





Stoichiometric amounts of Li_2CO_3 and NiO were mixed to obtain samples with nominal compositions of $x=0.15, 0.2, 0.25, 0.3, 0.4, 0.5, 0.6$. The mixture was mixed with ethanol and grounded by a ball-milling machine for 12 hours and then calcined at $850\text{ }^\circ\text{C}$ in air for 3 hours. The calcined powder was then pressed into disk pellets and sintered at $900\text{ }^\circ\text{C}$ for another 2.5 hours. The furnace was allowed to cool to room temperature at its natural cooling rate. The crystalline phases of the sintered pellets were characterized by XRD.

The SBN targets used in this research were fabricated by Mr. T. Y. Yum of our group using SrCO_3 , BaCO_3 and Nb_2O_5 powders. The detailed procedures had been reported by other group. [J. Zhu *et al*]

4.2.2 XRD Characterization

Figure 4.2 shows the θ - 2θ scans of LNO targets with different lithium compositions of 15%, 20%, 25%, 30%, 40%, 50% and 60%. From the profiles, we notice that all the peaks are at the same positions. They correspond to the cubic structure of LNO according to the x-ray database. This means that all the



LNO targets are in a cubic structure. However, from the profiles of LNO50 and LNO60, in which the cubic structure is still maintained, a weak peak identified as the (111) peak of Li_2O phase is also identified. Our XRD results show that, even with lithium content up to 60%, the LNO target still maintain a cubic structure. This might due to small atomic weight of lithium element. It evaporates easily during the fabrication process. Indeed, even with 60% of lithium in the initial composition, it would only form small amount of Li_2O , making the LNO target in cubic structure.

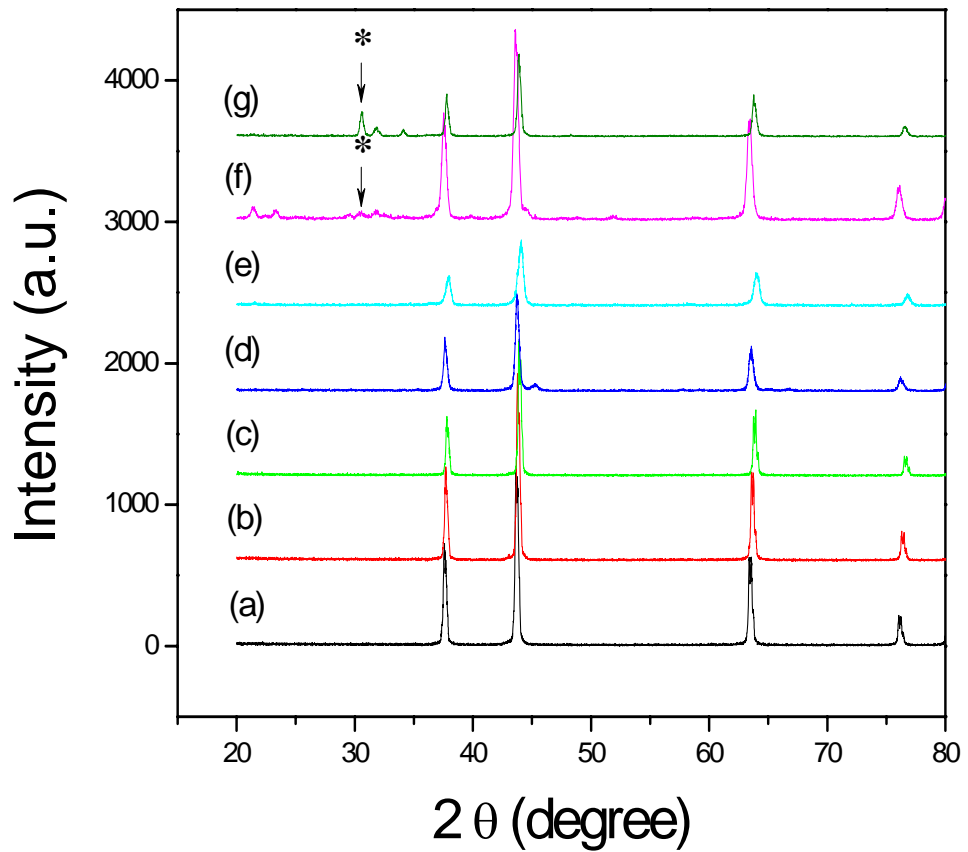


Figure 4.2 θ - 2θ scan profiles of LNO targets with different Li contents of (a)

LNO15; (b) LNO20; (c) LNO25; (d) LNO30; (e) LNO40; (f) LNO50 and (g)

LNO60. The (111) Li_2O peak is denoted by asterisk (*)



4.3 Fabrication and Characterization of LNO Films

The oxygen pressure inside the deposition chamber has been shown to be an important processing parameter of the deposition of LNO film. [S-J. Wen *et al.*] They reported that the surface of the films deposited under a lower oxygen pressure of 60 mTorr is smoother than that of the films deposited under a higher oxygen pressure of 200 mTorr due to the fact that higher particle energy would increase the surface mobility to produce a smoother film. Similarly, the Li/Ni and Li/O ratios, which strongly affect the electrical conductivity of the LNO films, are also increased with the oxygen pressure. On the other hand, the Ni/O ratio decreases with the oxygen pressure below 100 mTorr and then keep stable above 100 mTorr. Therefore, considering both the surface morphology and conductivity property, oxygen pressure of 100 mTorr was employed in our studies.

4.3.1 Fabrication of the LNO Films with Different Li Contents

LNO films with different initial Li concentrations were grown on (001) MgO



substrates by PLD. A KrF excimer laser operating at 248 nm with pulse width of 10 ns was focused on the rotating target. The distance between the target and the substrate was 40 mm. Laser repetition rate of 10 Hz and power density of 4 J/cm² were employed. In order to find the optimum substrate temperature, deposition of LNO films was carried out using substrate temperatures of 550, 600 and 650 °C, in an oxygen ambient pressure of 100 mTorr with different deposition times. The as-deposited film was post-annealed at the deposition temperature and pressure for another 10 minutes. Finally, the sample was cooled down to room temperature naturally. The typical film thicknesses were about 90, 150 and 200 nm for deposition times of 5, 10 and 15 minute, respectively.

The structural properties and surface morphologies of the films were characterized by X-ray diffraction (XRD) and scanning electron microscopy (SEM), respectively. To determine the actual lithium composition in the LNO films, X-ray photoelectron spectroscopy (XPS) was employed. Optical transmission (OT) and refractive index were determined by an UV-visible spectroscopic system and spectroscopic ellipsometry (SE), respectively.



4.3.2 Structural Characterization and Surface Morphology of the LNO Films

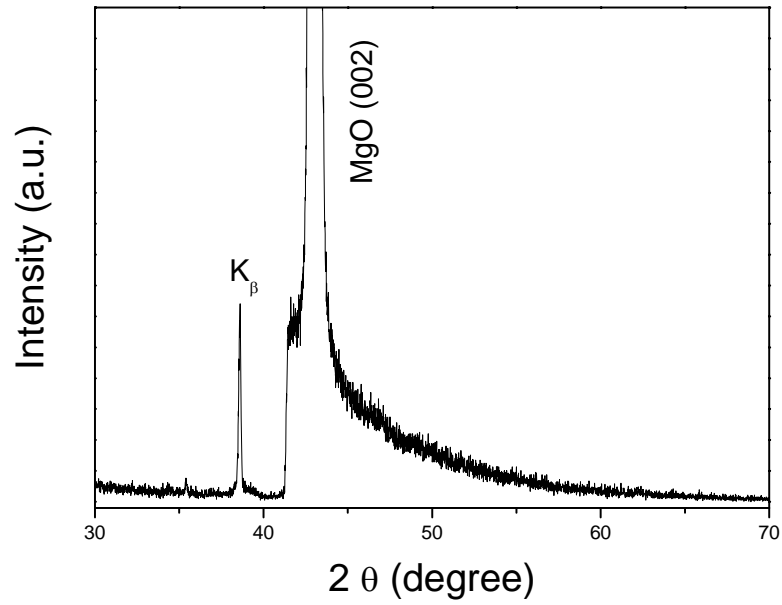
Figure 4.3 plots the θ - 2θ XRD profiles of LNO films (with Li content of 40%) deposited at different substrate temperatures. Similar trends are observed in all the films with different Li compositions. For films deposited above 550 °C, only LNO (002) peak is clearly identified, indicating that the films are single phase and *c*-axis oriented with a cubic structure corresponding to $\text{Li}_x\text{Ni}_{1-x}\text{O}$.

The out-of-plane lattice constants calculated from the (002) diffraction peak of LNO films deposited at 600 °C and 650 °C are 0.413 and 0.416 nm, respectively. The full-width at half-maximum (FWHM) obtained from the rocking curve of the LNO (002) peaks of 600 and 650 °C deposited films are 0.58° and 0.45°, respectively. As a comparison, the FWHM of the MgO substrate is 0.3° due to limitation of our equipment. However, for the film deposited at 550 °C, no LNO peaks are found. This indicates that below 550 °C, the films do not crystallize well. XRD ϕ scans, shown in Figure 4.4, were performed in order to confirm the growth quality of the epitaxial films. For both the films produced at 600 and 650 °C, the LNO (111) and MgO (111)

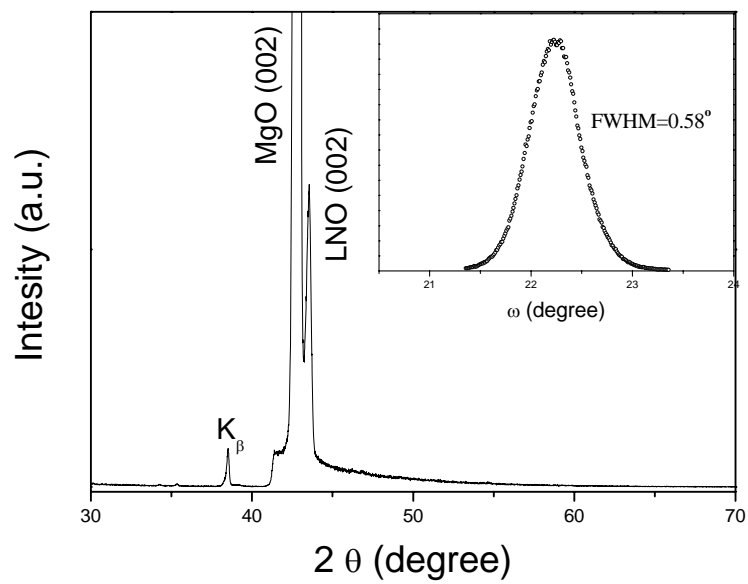


diffraction peaks appear at the same degrees with a 90° separation due to their four-fold symmetry. This confirms that our LNO films are cube-on-cube grown on the MgO substrates. Our XRD results indicate that crystalline quality of LNO film improves with increasing substrate temperature and the film can be epitaxially grown on MgO substrate with an in-plane epitaxial relationship of $(001) \text{ LNO} \parallel (001) \text{ MgO}$ above 600°C .

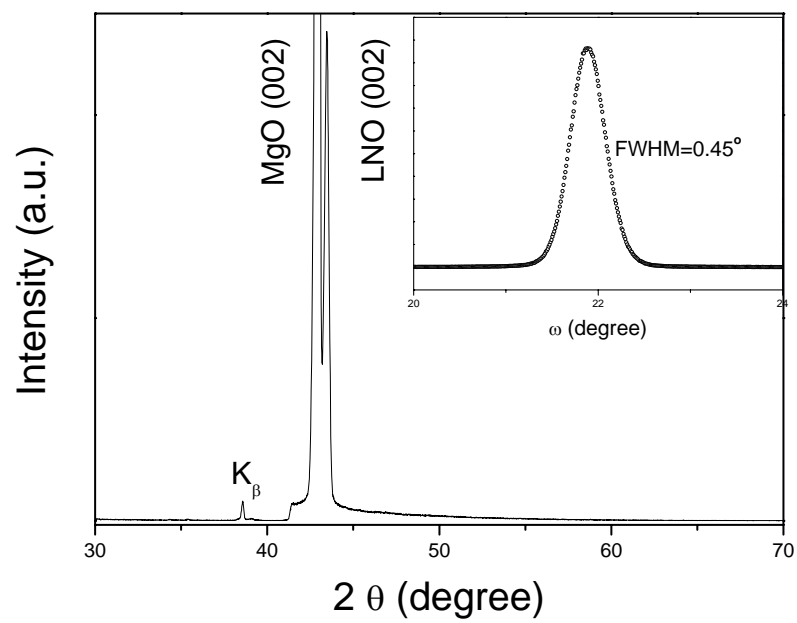
The θ - 2θ scans of LNO films with different Li contents were plotted in Figure 4.5. From the figure, we found that all the LNO films are single phase with a cubic structure. The diffraction intensity of LNO (002) peaks increases with Li contents. The preferred cubic phase is probably due to the confinement arisen from the MgO substrate. Also, we notice that LNO50 and LNO60 films have the similar profiles (not shown) except the intensity of LNO peak was weaker than that of LNO40. They still maintain a cubic structure with the observation of some weak peaks identified as the Li_2O phase. This implies that the excessive lithium might form Li_2O in the LNO50 and LNO60 films.



(a) deposited at 550 °C



(b) deposited at 600 °C



(c) deposited at 650 °C

Figure 4.3 θ - 2θ profiles of LNO40 films deposited at different substrate

temperatures of (a) 550 °C, (b) 600 °C and (c) 650 °C.

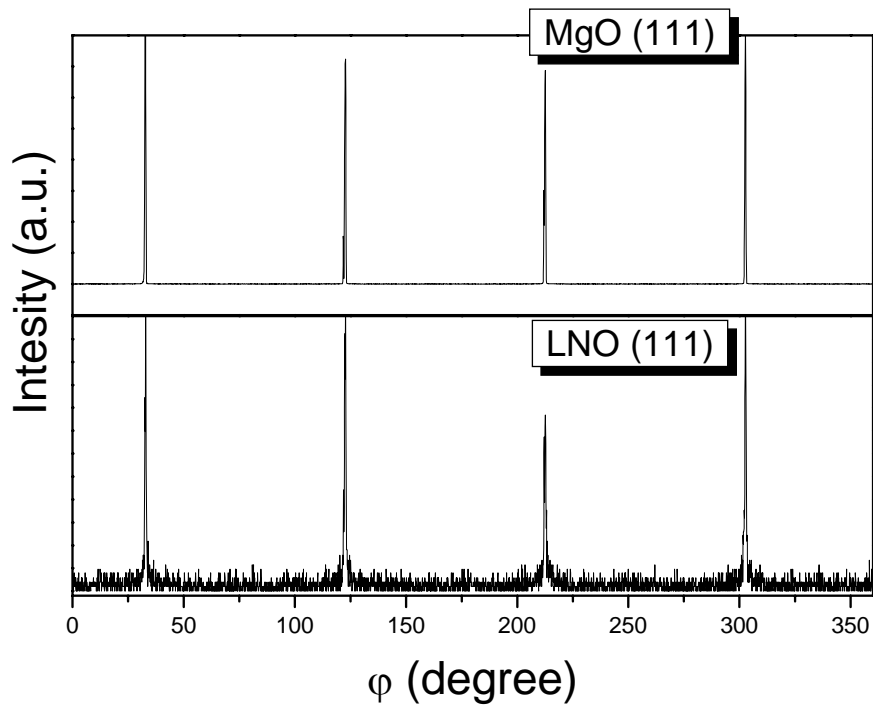


Figure 4.4 ϕ scan profiles for the LNO (111) and MgO (111) planes

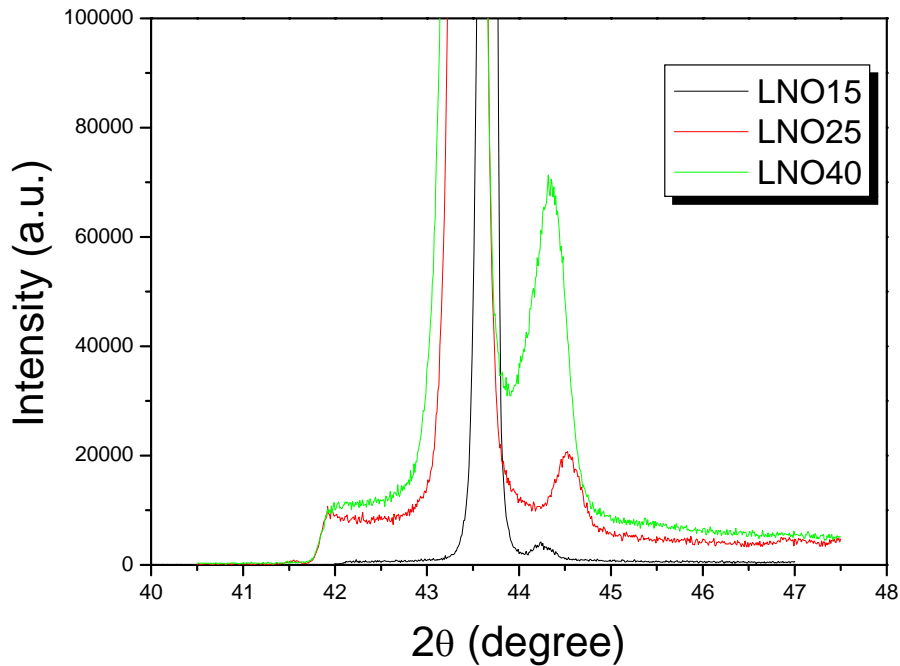


Figure 4.5 θ - 2θ scans of LNO films with different Li contents

The surface and cross-section SEM micrographs of LNO films with different Li contents are shown in Figure 4.6. Figure 4.6(a) shows a smooth, dense and crack-free surface, indicating the good surface qualities of our films. From the cross-section micrograph, LNO layer with columnar structure on top of the substrate is clearly identified. The thicknesses of the LNO films deposited at different duration times are estimated to be 90, 150 and 200 nm for 5, 10 and 15 minutes, respectively.

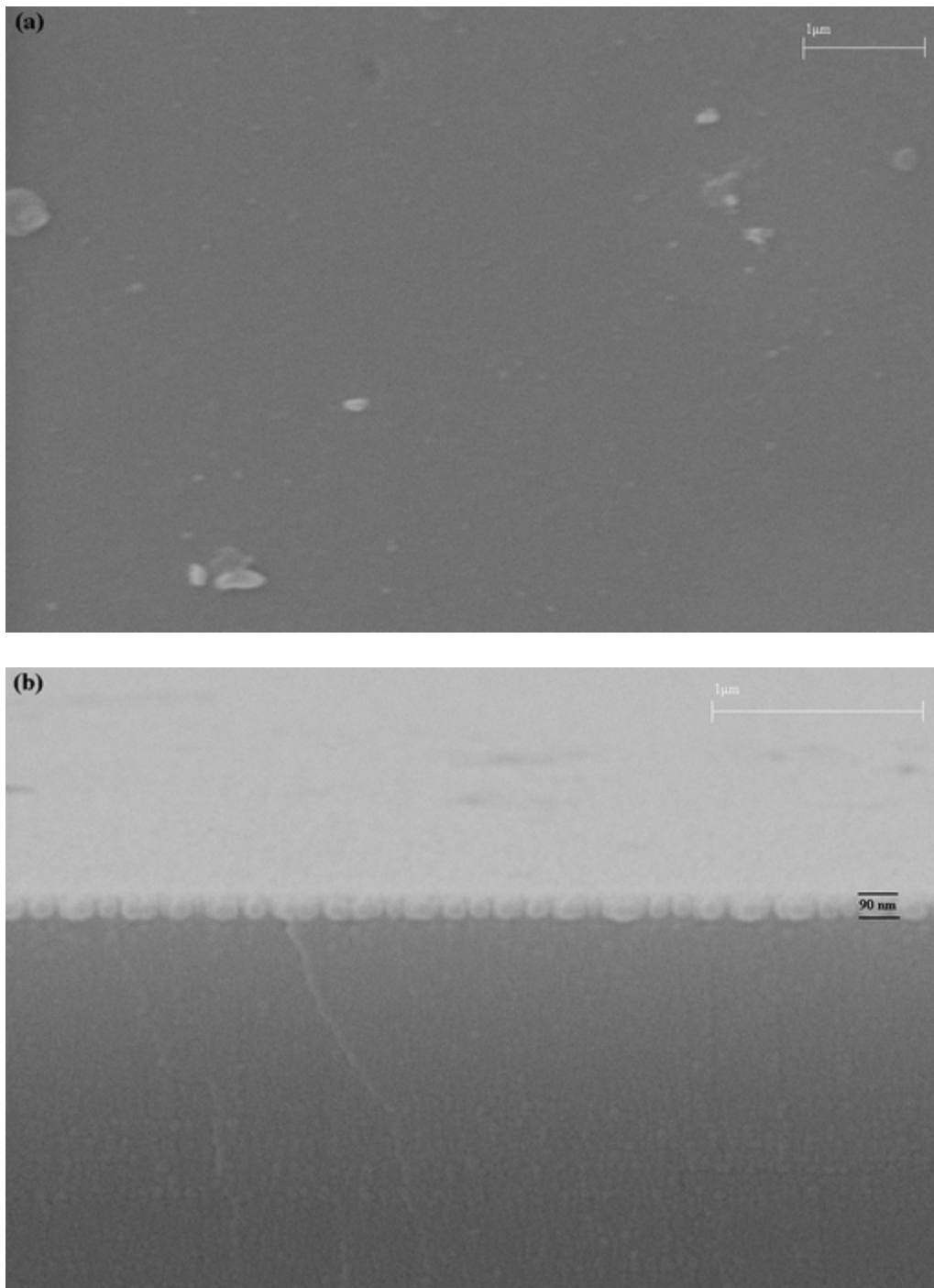


Figure 4.6 SEM micrographs of the (a) surface and (b) cross-section views of

LNO40 film deposited on MgO substrate for 5 minutes



4.3.3 Characterization of the Lithium Content of the LNO Films

Figure 4.7 shows the lithium concentration measured by XPS in the as-deposited LNO films as a function of the starting chemical composition of $\text{Li}_x\text{Ni}_{1-x}\text{O}$. From the XPS results, we observe that remained Li content are 2.1%, 4.0%, 5.4%, 6.5% and 7.2% in the films of LNO15, LNO20, LNO25, LNO30 and LNO40, respectively. These films were all deposited at a substrate temperature of 600 °C. T. Kamiya *et al* reported that approximately 75% of lithium should evaporate from the growth surface of the LNO film deposited at room temperature. Considering the loss of lithium during the heat treatment in the target fabrication process as well as our higher substrate temperature, we believe that our results are in good agreement with the previous report.

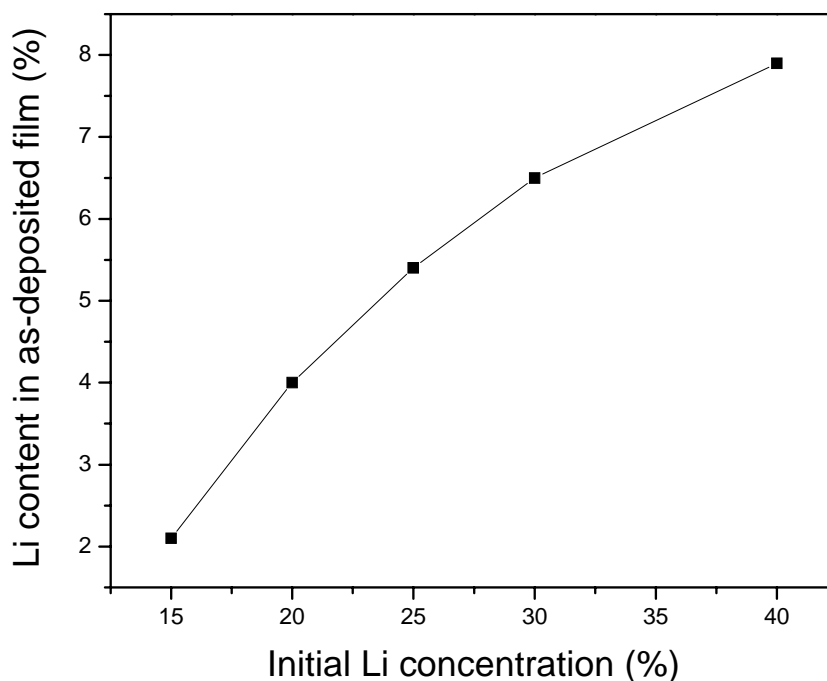


Figure 4.7 Li concentration in as-deposited LNO films as a function of the initial Li composition of $\text{Li}_x\text{Ni}_{1-x}\text{O}$

4.3.4 Resistivity of LNO Films

When Li^+ ions substitute the normal sites of Ni^{2+} ions, in order to keep charge neutral, holes in form of Ni^{3+} or O^- are introduced. As a result, the resistivity drops off. This means that the resistivity of LNO decreases with an increase in lithium content. Figure 4.8 plots the variation of the resistivity of our



as-deposited LNO films with different lithium contents. The films were deposited at the substrate temperatures of both 600 °C and 650 °C. It was observed that, for the same initial Li content, the films deposited at a lower substrate temperature exhibit a lower resistivity due to a higher Li content existing in the films. On the other hand, for fixed deposition temperature, it was noticed that the LNO40 ($x = 0.4$) film seizes the lowest resistivity which is an order of magnitude less than that of the LNO15 film. In general, we expect that a higher Li content would result in a low resistivity of the film. However, from our XRD measurements (Figure 4.3), we noticed that although the LNO50 and LNO60 films still maintain a cubic $\text{Li}_x\text{Ni}_{1-x}\text{O}$ structure, some Li_2O phase also co-exists in the films. The preferred cubic phase is probably due to the confinement arisen from the MgO substrate; while the excessive lithium in the film might form the insulating Li_2O phase. Thus, the resistivity of the films increases. As shown in the next section, all LNO films have no observable difference in their optical transmission spectra. Therefore, from the viewpoints of the structural, optical and conductivity properties, 600 °C deposited LNO40 films have been used as both the bottom electrode and buffer layer throughout our studies.

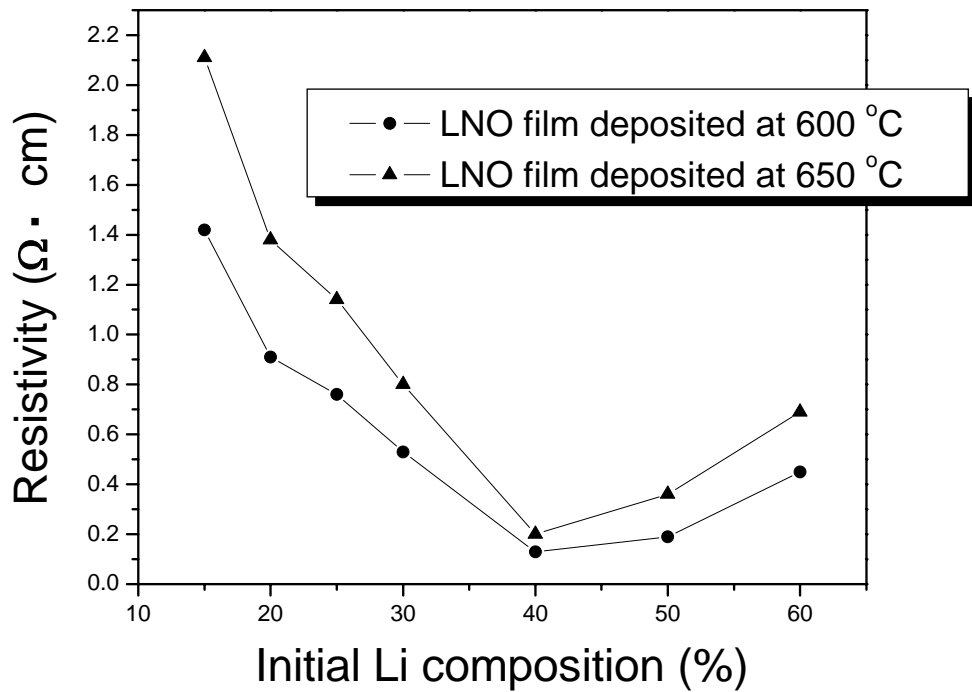


Figure 4.8 Resistivity of as-deposited LNO films with different initial Li contents

4.3.5 Optical Transmittance and Refractive Index Measurements of LNO Films

Figure 4.9(a) shows the optical transmittance spectra of LNO films with different lithium contents. All of the LNO films with different Li contents or thickness exhibit similar shapes and trends in their optic transmission spectra



and drop at the same position. LNO40 film deposited for 10 minutes possesses the highest optical transmittance of about 40% among these LNO films so that it was used in our studies.

The optical band-gap energy of our thin films was deduced from the spectral dependence of the absorption constant $\alpha(\lambda)$ by applying the Tauc relation:

$$\alpha(\lambda)hv = B(hv - E_{gap})^{1/r} \quad (\text{Eq. 4.1})$$

where B is a constant and E_{gap} is the band-gap energy. $r = 2$ for direct allowed transition. The absorption constant $\alpha(\lambda)$ was determined from each transmittance spectrum using an extrema (or minima) envelope method described in detail elsewhere [Davis E.A. *et al*]. $\alpha(\lambda)$ is given by

$$\alpha(\lambda) = \frac{\ln(1/T)}{d} \quad (\text{Eq. 4.2})$$

in which T is the transmittance and d is the film thickness. The optical bandgap energy was obtained from Eq. (1) by extrapolation of the linear portion of the plot of $(\alpha hv)^2$ versus hv to $(\alpha hv)^2 = 0$. Figure 4.9(b) plots $(\alpha hv)^2$ as a



function of $h\nu$ for LNO films grown on MgO substrates. The optical bandgap energy was found to be in the range of 3.16~3.21 eV for all the LNO thin films.

The refractive indices n of the LNO films was measured by spectroscopic ellipsometry (Jobin Yvon). Figure 4.10 show the dispersion curves of both n and extinction coefficient k . From the figure, we notice that n is about 1.75~2.0 in the wavelength range of 400-550 nm. This refractive index range is in a good agreement with that of 1.75~1.9 obtained by S-J. Wen *et al.* and is still larger than the value of 1.73 of MgO substrate. Furthermore, it is also much lower than the value of about 2.28 of SBN single crystal. Therefore, waveguide structure can be obtained by depositing SBN/LNO on MgO substrate.

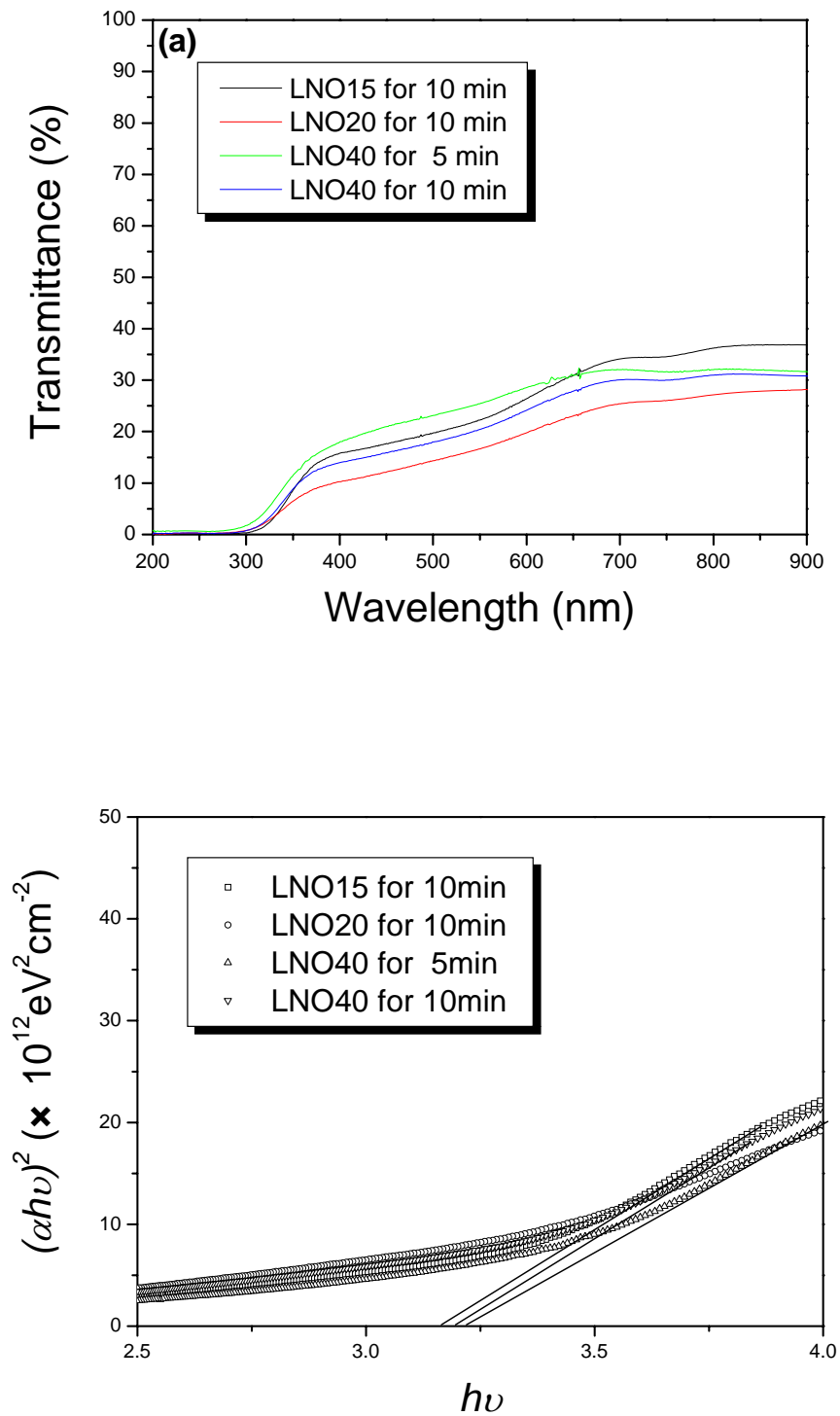


Figure 4.9 The (a) optical transmittance spectra and (b) optical band-gap energy

of LNO films with different Li contents and different film thickness

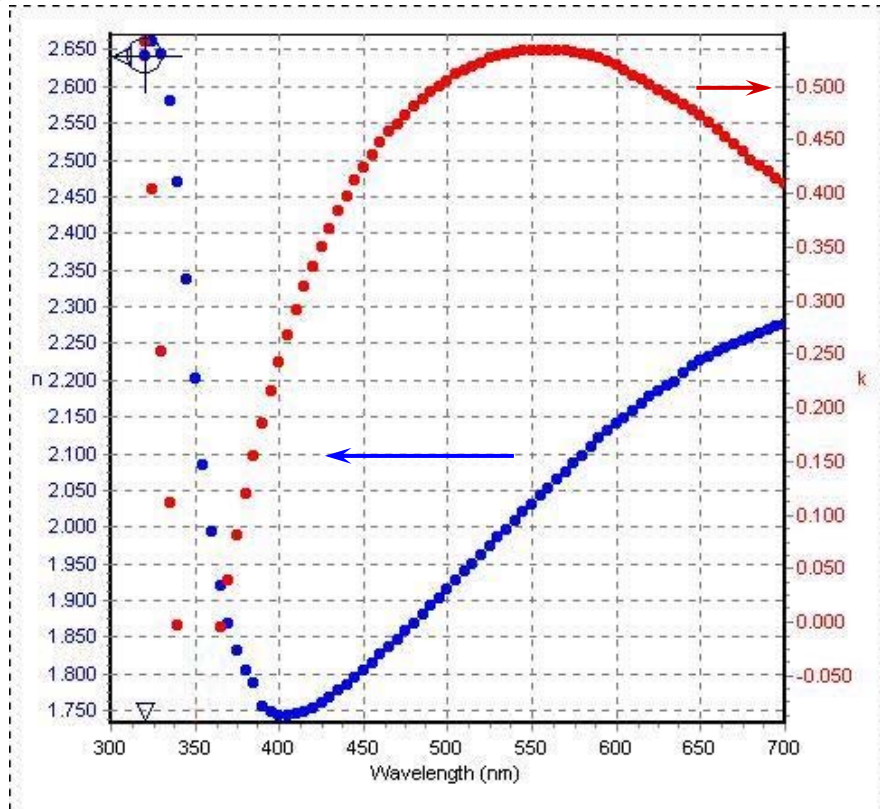


Figure 4.10 Refractive index measurement of LNO40 film deposited on MgO substrates by spectroscopic ellipsometry

From sections of 4.3.4 and 4.3.5, the LNO40 films possess the lowest resistivity among all different Li-composition LNO films, while all transmission profiles of these films are about 40% in the visible range. Based on the conductivity and transmission considerations, LNO40 films were chosen as the bottom electrode in our SBN/LNO structures which are described in the next section.



4.4 Fabrication and Characterization of SBN/LNO

Heterostructures

4.4.1 Fabrication of SBN/LNO Films on MgO Substrates

SBN/LNO heterostructure were grown on (001) MgO substrates by pulsed laser deposition (PLD). A KrF excimer laser operating at 248 nm with pulse width of 10 ns was focused on the rotating target. The distances between the targets and the substrates were 40 mm and 45 mm for LNO and SBN films, respectively. Laser repetition rate of 10 Hz and power density of 4 J/cm^2 were employed. Deposition of LNO films was carried out with a substrate temperature of $600 \text{ }^\circ\text{C}$ in an oxygen ambient pressure of 100 mTorr for 10 minutes while for the SBN films, 200 mTorr was used. To suppress the Li-evaporation, the SBN layers were deposited using a two-step process. A very thin SBN layer was first deposited at a substrate temperature of $600 \text{ }^\circ\text{C}$ for 3 minutes. Subsequently, a thicker SBN layer was deposited at a higher substrate temperature of $730 \text{ }^\circ\text{C}$ for another 37 minutes. All as-deposited films were post-annealed at the deposition temperature and pressure for 10 and 15 minutes for LNO and SBN films,



respectively. Finally, the sample was cooled down to room temperature naturally. The typical film thicknesses were 150 and 600 nm for LNO and SBN layer, respectively.

The structural properties and surface morphology of the films were characterized by X-ray diffraction (XRD) and scanning electron microscopy (SEM), respectively. To measure surface roughness of the films, atomic force microscopy (AFM) was employed. Optical transmission (OT) and wave-guiding property were determined by an UV-visible spectroscopy system and a coupling prism technique, respectively.

4.4.2 Structural Characterization and Surface Morphology of the SBN/LNO Films

XRD θ - 2θ scan patterns of the SBN/LNO/MgO heterostructure are shown in Figure 4.11. Only SBN (001), LNO (002) and SBN (002) peaks are observed, indicating that all the films are single phase and highly *c*-axis oriented. The peak appears at angle between 25° and 30° , which was also observed from the XRD profile of pure MgO substrates, is due to the equipment problem. The



calculated lattice constants are $c = 0.395$ nm for SBN and $c = 0.416$ nm for LNO, which are in good agreement with the reported values. The full-width at half-maximum (FWHM) obtained from the rocking curve of the SBN (002) peak and LNO (002) peak are 0.66° and 0.51° , respectively. As a comparison, the FWHM of the MgO substrate is 0.21° due to our equipment limitation. To verify the epitaxial growth of the films, ϕ scans are plotted in Figure 4.12(a). The LNO (111) and MgO (111) diffraction peaks appear at the same degrees with a 90° separation due to their four-fold symmetry. This confirms that the LNO films are cube-on-cube grown on MgO substrates. The diffraction peaks on the SBN (221) plane, however, show two sets of peaks. This indicates that the anti-phase domains in the SBN films are aligned at either $\pm 18.8^\circ$ or $\pm 30.5^\circ$ with respect to the reflection of the MgO (100) plane. From the ϕ scans data, the orientation relationship between the SBN and LNO/MgO can be described as (100) SBN \parallel (310) LNO/MgO and (100) SBN \parallel (350) LNO/MgO. [Youden K. E. *et al.*] Figure 4.12(b) shows a $z=0$ plane of SBN with the (100) direction rotated by 18.8° with respect to the (100) direction of MgO.

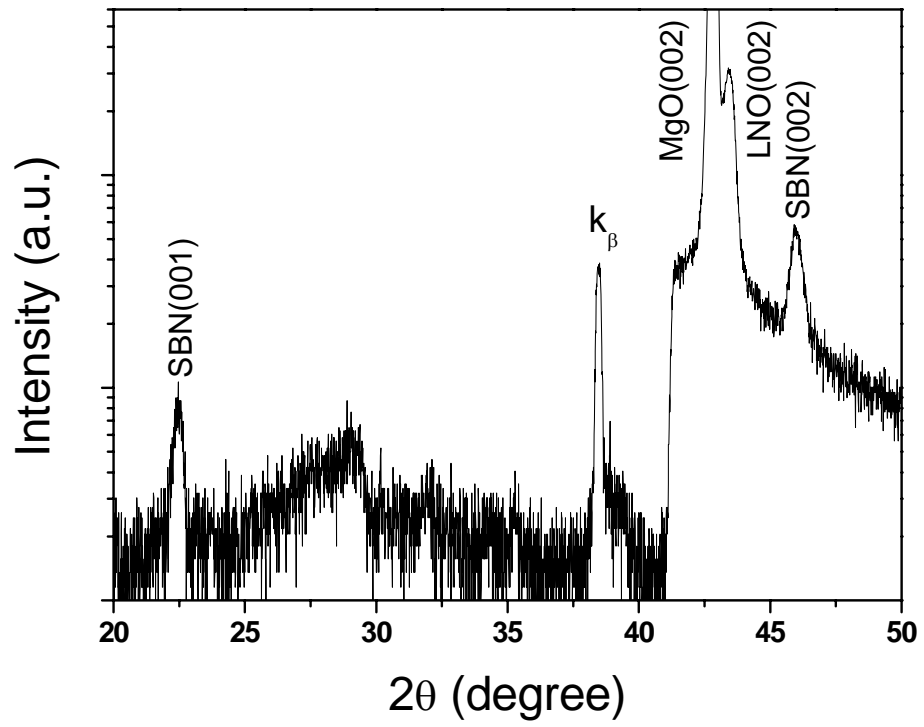


Figure 4.11 θ - 2θ scan pattern of the SBN/LNO heterostructure deposited on

MgO substrate

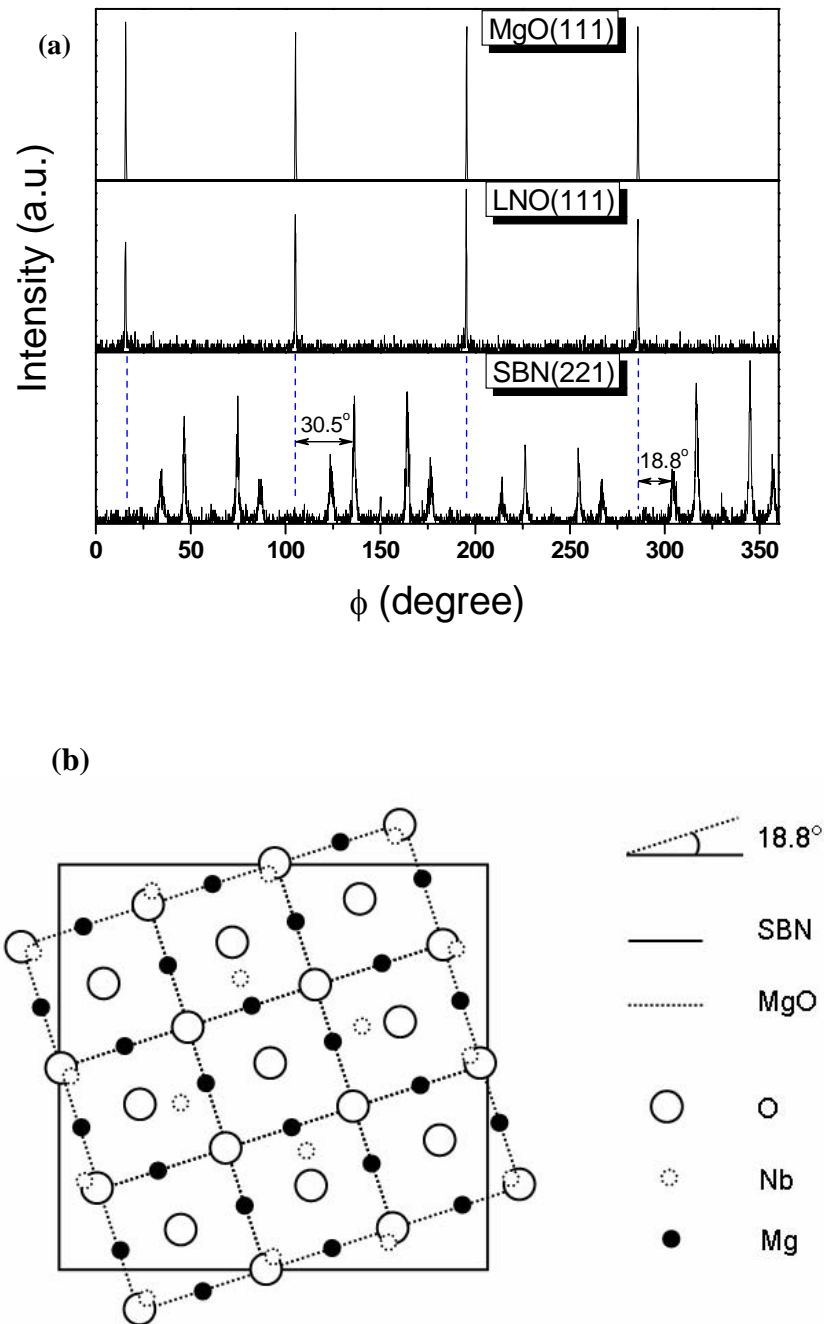


Figure 4.12 (a) The X-ray diffraction ϕ scan patterns on the planes of MgO (111), LNO (111) and SBN (221); (b) SBN (100) rotated by 18.8° with respect to MgO (100) showing the $z=0$ plane of SBN.



To investigate the effect of LNO layer on the growth of the SBN films, we deposited SBN films on MgO substrates with and without LNO layer under the same pressure at different substrate temperatures. The XRD patterns of the three different SBN films are shown in Figure 4.13. Our results indicate that SBN film is crystallized on LNO layer at a deposition temperature as low as 710 °C; while it is only crystallized at a higher temperature of 750 °C without the LNO layer. This implies that LNO layer can effectively promote the crystallization of SBN films on MgO substrate at a lower deposition temperature. This promotion might be due to the similar lattice constants of LNO layer (~0.416 nm) with those of SBN films (~0.395 nm) and MgO substrates (~0.421 nm). Hence, the lattice mismatch decreases from a value of 6.2% between SBN and MgO to that of 5.0% between SBN and LNO.

The SEM micrographs shown in Figure 4.14 display the surface and cross-section morphologies of the SBN/LNO/MgO heterostructure. The surface micrograph shows a smooth, dense and crack-free surface, indicating a good surface quality of our films. From the cross-section micrograph, two prominent layers with columnar structures on top of the substrate are clearly identified.

The thicknesses of the LNO and SBN layers are estimated to be 150 nm and 600 nm, respectively.

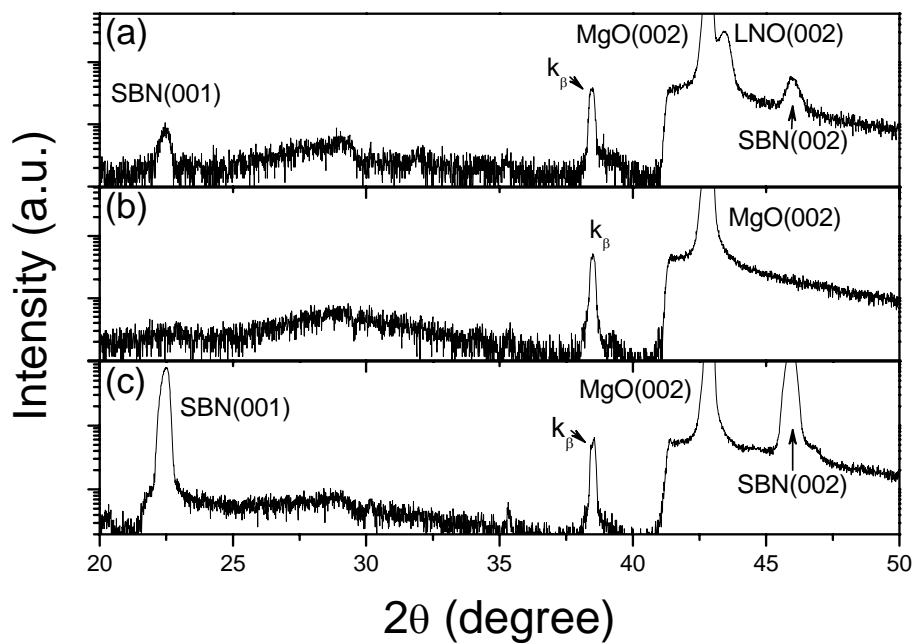


Figure 4.13 θ - 2θ scan patterns of the SBN films deposited on MgO substrates (a) with LNO layer deposited at 710 °C; (b) without LNO layer deposited at 730 °C and (c) without LNO layer deposited at 750 °C.

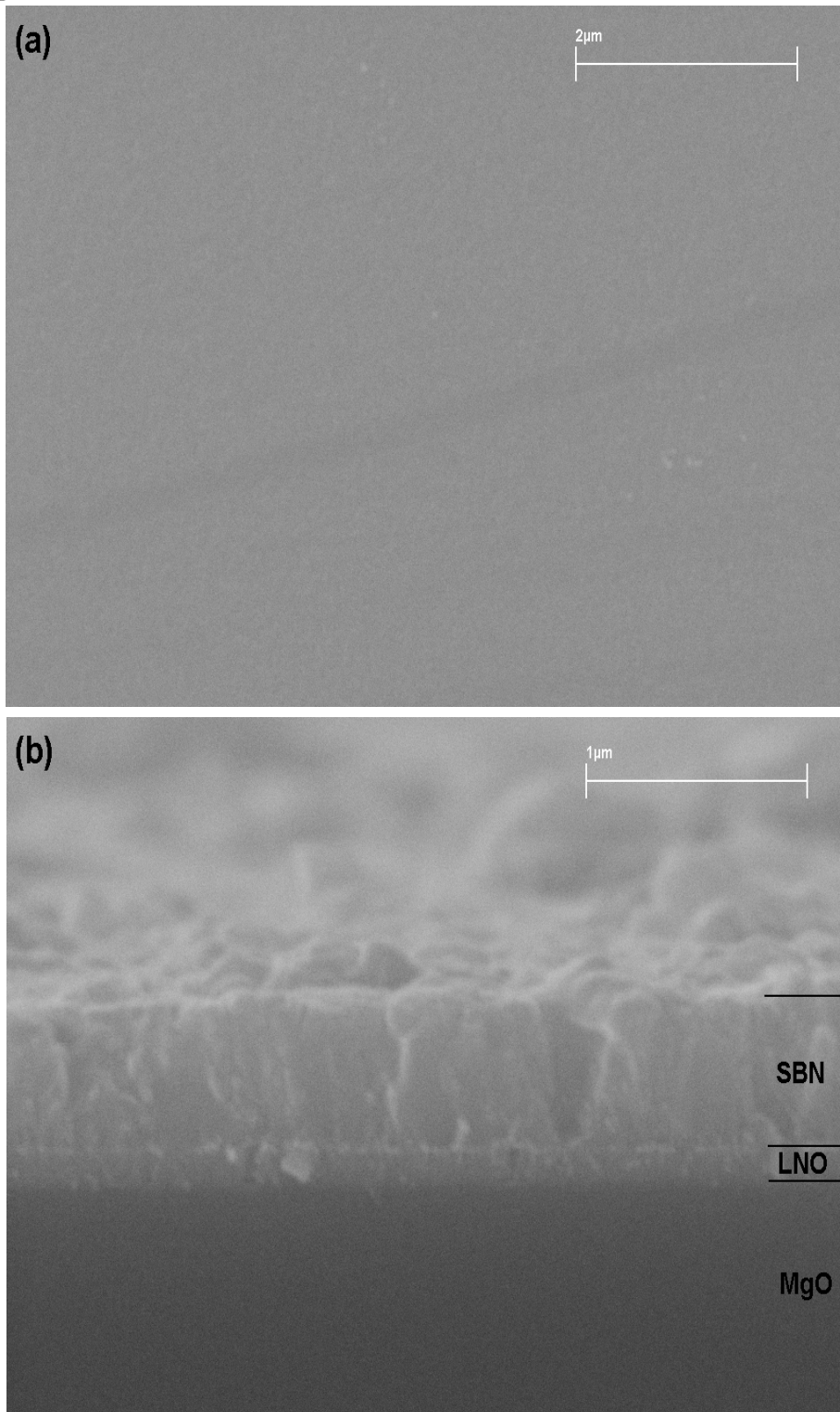


Figure 4.14 The SEM (a) surface and (b) cross-section micrographs of

SBN/LNO films grown on MgO substrates



4.4.3 Resistivity of LNO Layer before and after the Two-Step

Deposition Process of SBN Films

In order to demonstrate that the two-step process can effectively suppress the Li-evaporation, we deposited SBN films on LNO layers using both the two-step process and the conventional one-step process. Table I shows the resistivity of these films. From the table, it is revealed that the two-step deposition process effectively minimizes the resistivity change of the bottom LNO layer. This is probably due to the fact that the low-temperature SBN layer effectively suppresses the Li-evaporation at higher temperature. Further experiments will be required to verify the exact content of the LNO layer after the deposition of SBN.



	Resistivity of as-deposited LNO film ($\Omega\cdot\text{cm}$)	Resistivity of LNO film after the deposition of SBN films ($\Omega\cdot\text{cm}$)
Two-step process	0.132	0.468
Conventional one-step process		>2.4

Table I Resistivity measurements of as-deposited LNO film and LNO film after the deposition of the SBN layer using the two-step and conventional one-step processes.

4.4.4 Optical Transmittance Measurement of the Heterostuctures

The optical transmittance spectra are shown in Figure 4.15(a). To identify the transmission of LNO film after the deposition of SBN layer, the transmittance spectrum of SBN film deposited on MgO substrate under the same conditions



was also measured in order to act as a reference in the measurement of the transmittance profiles of LNO film. It is noticed that the optical transmittance in the visible range increases from 40% of the as-deposited LNO film to about 65-70% of the LNO film after deposition of SBN layer using the two-step process. For MgO and SBN films, the transmittances both are about 90%. Our results show that the high temperature annealing of the LNO film during the deposition of the SBN layer can effectively improve the optical transmission of the bottom LNO layer. This result is similar to that reported by Kamiya *et al.* We believe that LNO layer with even higher transmittance can be obtained by optimizing the processing parameters of the two-step process such as the low temperature SBN deposition period and the SBN deposition temperature etc.

The optical band-gap energy was obtained from Eq (1) by extrapolation of the linear portion of the plot of $(\alpha hv)^2$ as a function of hv to $(\alpha hv)^2=0$. Figure 4.15(b) shows $(\alpha hv)^2$ versus hv for LNO and SBN film grown upon MgO substrate. The optical band-gap energy of the LNO film after SBN deposition increased from 3.19 (see Figure 4.9(b)) to 3.72 eV and that of SBN thin films deposited on MgO substrates was 4.30 eV, respectively.

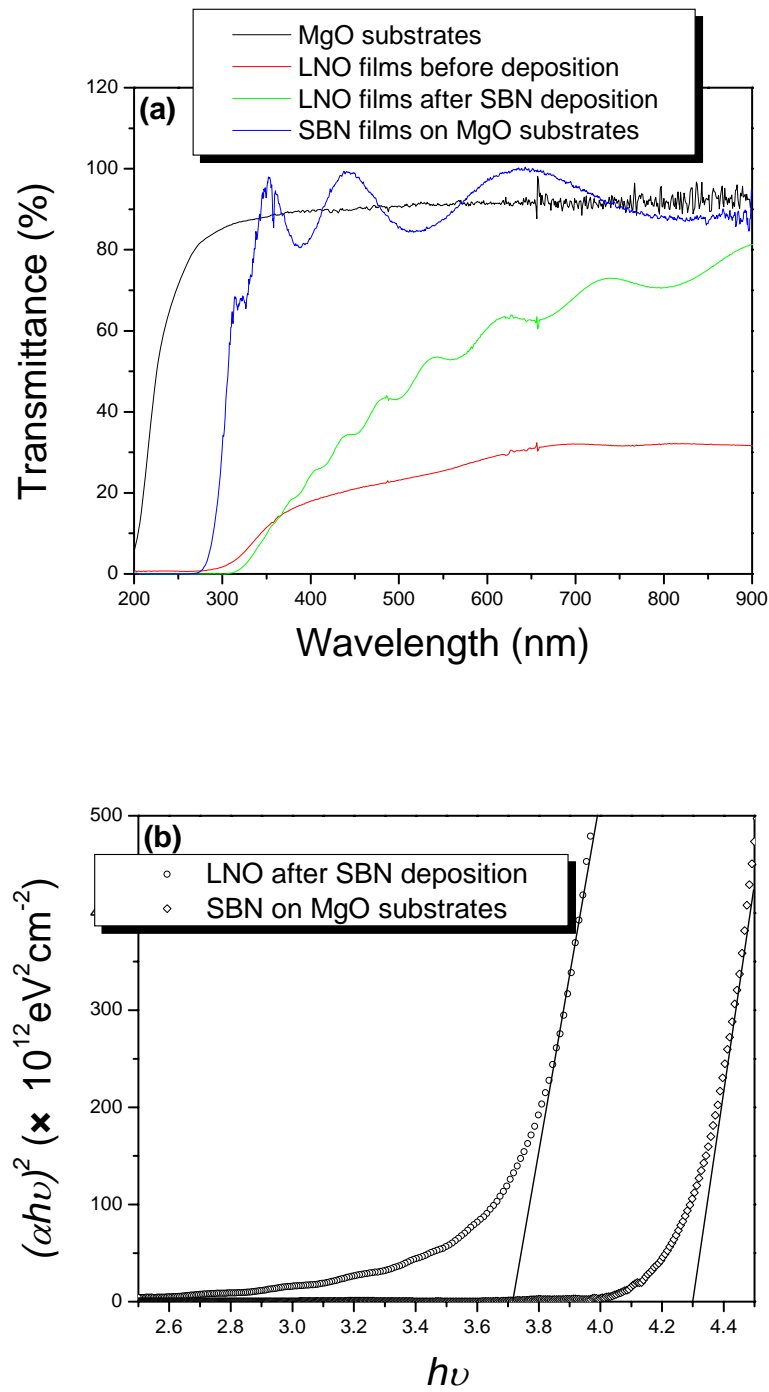


Figure 4.15 The (a) optical transmittance spectra and (b) optical band-gap energy of MgO substrates, SBN film, as-deposited LNO film and LNO film after SBN deposition



Although the SBN film has been fabricated at lower temperature by buffered a transparent conductive LNO layer using the two-step deposition process, it exhibits poorer crystalline structure compare with the film deposited on MgO substrate. This might due to a lower density and poor morphology of our LNO film resulted from a little of Li-evaporation. Therefore, the waveguide properties of SBN/LNO/MgO structure have not been obtained yet. These studies will be performed in the future by improving the LNO fabrication.

4.4.5 Waveguide Properties of the SBN Films

To characterize the waveguide properties of SBN film grown on (001) MgO substrate, a prism coupling technique was performed at a wavelength of 632.8 nm. Figure 4.16 shows the guiding mode spectra (*m*-line) of SBN film with thickness of about 600 nm. In the figure, three TE (transverse electric) modes and three TM (transverse magnetic) modes are observed. All of the mode-lines are sharp and distinguishable, indicating that a good confinement of light propagation is achieved and the film is potentially useful for optical waveguide devices. In the prism-film coupling method, at certain discrete incident angles,



called mode angles, photons can tunnel across the air gap to form an optical propagation waveguide mode. This causes a sharp drop in the intensity of light reaching the detector. Indeed, the measured n_{TE} and n_{TM} represent the ordinary refractive index n_o and the extraordinary refractive index n_e of the films, respectively. Following Ulrich and Torge, the refractive index and thickness of waveguide films can be calculated using the following equations.

$$\begin{aligned} N_m &= \sin \alpha_m \cos \varepsilon + (n_p^2 - \sin^2 \alpha_m)^{1/2} \sin \varepsilon \\ 2\pi h(n^2 - N_m^2)^{1/2} / \lambda &= m\pi + \phi_0(n, N_m) + \phi_2(n, N_m) \quad (\text{Eq. 4.3}) \\ \phi_i(n, N_m) &= \tan^{-1} \left[\left(\frac{n}{n_i} \right)^{2\rho} \left(\frac{N_m^2 - n_i^2}{n^2 - N_m^2} \right) \right]^{1/2} \end{aligned}$$

where m represents the m th mode, $\rho=0$ for TE modes and $\rho=1$ for TM modes. $i=0, 2$. λ is the wavelength of the laser. n_p is the refractive index of prism. α_m is the coupling mode angle of the m th mode. ε is a constant of 44.98° , determined by the type of the prism. h is the thickness of the waveguide layer. n_0 , n , and n_2 are refractive indices of the air gap, the waveguide layer, and the cladding layer, respectively.

From our measured data, the ordinary refractive index n_o (n_{TE}) and the



extraordinary refractive index n_e (n_{TM}) of SBN film were calculated to be 2.1843 and 2.1684, respectively. Both these refractive indices are smaller than those of bulk SBN ($n_o = 2.312$ and $n_e = 2.281$). This might be due to a lower density of our SBN films as compared to that of SBN single crystal. It should be noted that there is a relatively small index difference of $\Delta n = n_o - n_e = 0.0159$. The small birefringence in this SBN film on MgO substrate is probably due to the existence of other orientations in the films which definitely reduces the Δn value. The thicknesses of the SBN film were determined to be 608 nm and 627 nm from the TE and TM mode, respectively, which are in good agreement with those obtained by SEM.

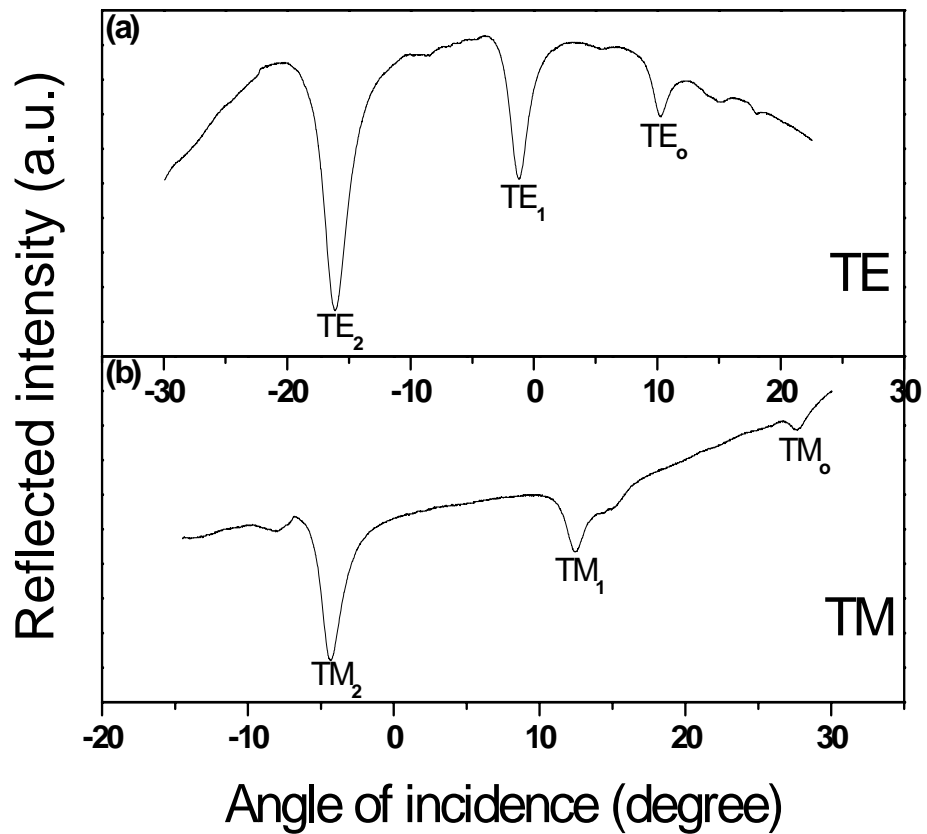


Figure 4.16 The (a) TE-line and (b) TM-line spectra for the air/SBN/MgO

waveguide structure on MgO substrates



The optical propagation loss of the film can be evaluated by the following equation:

$$\delta(\text{dB/cm}) = \frac{\ln(P_2/P_1)}{Z_1 - Z_2} = 4.3\alpha \quad (\text{Eq. 4.4})$$

where α is the decay coefficient for optical propagation, P_1, P_2 represent the intensity of light scattered out from TM or TE modes at the propagation distances of Z_1 and Z_2 , respectively, and δ represents the propagation loss.

During the measurement of optical loss along the propagation direction, the prism coupler measures a series value of loss at different propagation distance, and then plots the loss as a function of the distance; therefore, the tangent of the line fitted from the experimental point can be determined as the decay coefficient α . Figure 4.17 shows the scattered light intensity from TM_0 mode of SBN films deposited on MgO substrates. According to the equation mentioned above, the propagation loss of our SBN films was calculated to be 3.45dB/cm. This value can be further decreased by optimizing the fabrication parameters.

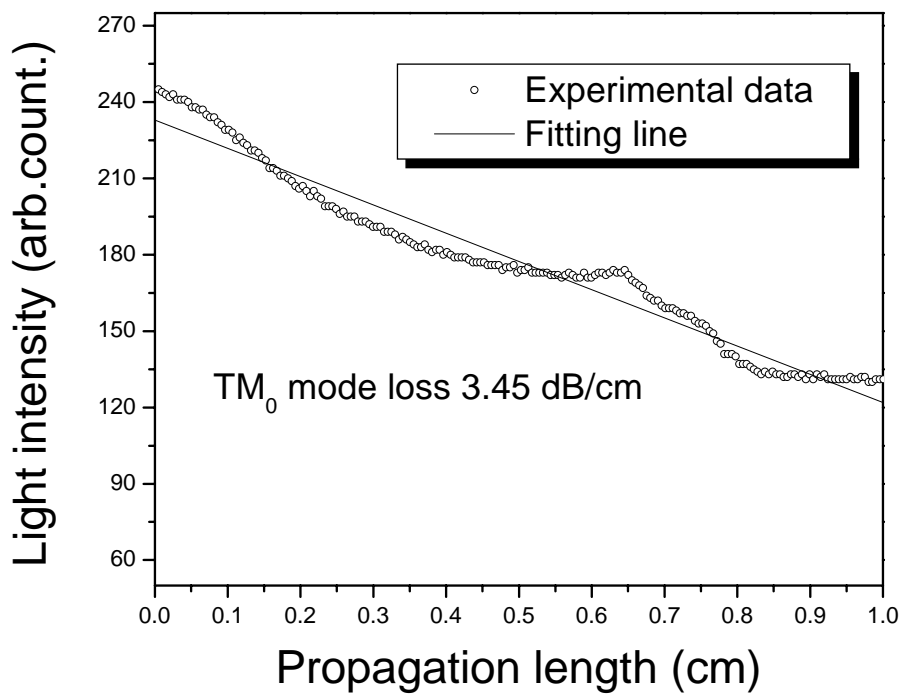


Figure 4.17 TM_0 mode scattered intensity of SBN film deposited on MgO

substrate



Chapter 5

Fabrication and Characterization of SBN Thin Films Grown on (001) Si Substrates Buffered by MgO/TiN Layer

5.1 Introduction

In recent years, the development of integrated optical devices has stimulated the demand for ferroelectric thin films. Optical waveguides provide a significant improvement in the efficiency of electro-optical (EO) and nonlinear optical applications which results from strong light beam in the guide structures. General speaking, a waveguide device is usually achieved by combining a ferroelectric thin film with high refractive index as the core layer and a low refractive index layer as the cladding layer. Due to the large refractive index difference, a very high light intensity per unit power in this guiding structure can be achieved, and hence, a large nonlinear effect within a short interaction length can be obtained. Among up-to-date researches, PLD fabricated SBN thin film for waveguide applications has attracted many interests because of its



compatibility with integrated optical devices and other miniaturized system.

Excellent waveguiding properties have been produced by some research groups through fabricating SBN films on single crystalline substrates. [Zhu Y. Y. *et al.*; Lee M. K. *et al.*]

Magnesium oxide (MgO) is an important material being a highly ionic insulator. It has NaCl-type structure and possesses low energy charge neutral {100} cleavage planes suitable for acting as substrates to grow perovskite structures. It has been demonstrated that many perovskite oxides can be epitaxially grown on MgO single crystal substrates. In addition, the refractive index of MgO (~1.735) is much smaller than other substrates such as yttria-stabilized zirconia (YSZ). The refractive index difference between SBN and MgO is about 0.5. Therefore, the combination of SBN thin film and MgO substrate is especially favourable for waveguide applications. However, the high cost of single crystal and poor compatibility with microelectronic devices limited the practical application of these waveguide devices. Silicon (Si), on the other hand, is the most suitable substrate because of its low price and wide utilization in the microelectronic technology. If we can combine the excellent waveguide structure with well developed silicon microelectronics, a new type of devices



correlating optical and microelectronics will be created. Chiu *et al.* fabricated epitaxial SBN films on Si substrates using $\text{LaNiO}_3/\text{CeO}_2/\text{YSZ}$ buffer layers. However, LaNiO_3 is not suitable to be used as a cladding layer for the waveguide structure because it decomposes easily. Both La and Ni tend to interdiffuse into SBN layer at high growth temperature of SBN. Based on the above considerations, in this project, the deposition of epitaxial SBN/MgO waveguide structure on Si substrate is valuable in terms of integrating optical system with microelectronic devices and replacing the expensive MgO single crystal substrates. Xiong *et al.* fabricated SBN films on Si substrates using SiO_2 or MgO as buffer layer. In their studies, only polycrystalline SBN films have been grown on (001) Si substrates. As we all know, epitaxial growth is important because it increases the EO effect, reduces the defects in the interface between films and substrates and decreases the optical propagation loss. Up to now, MgO films have been deposited on (001) Si substrates by various techniques, such as pulsed laser deposition (PLD), e-beam evaporation, metal organic chemical vapor deposition, molecular beam epitaxy and sol-gel method. However, the lattice constants of 0.421 nm and 0.543 nm for MgO and Si, respectively, result in a large lattice mismatch of $\sim 22.5\%$. This huge mismatch makes the growth of high quality epitaxial MgO films directly on Si substrates



to be difficult. This greatly affects the quality of SBN films subsequently deposited on MgO layer. In addition, there is a large difference in thermal expansion coefficients of Si of $4.0 \times 10^{-6}/^{\circ}\text{C}$ and that of MgO of $13.5 \times 10^{-6}/^{\circ}\text{C}$ which also creates a large thermal strain in the films. Therefore, a suitable buffer layer is required in order to grow a well-crystallized MgO films with atomically smooth surfaces on Si substrates.

Titanium nitride (TiN) possesses a NaCl-type structure consisting of Ti atoms filled into the f.c.c.-based lattice with all octahedral sites filled with nitrogen atoms. Its lattice constant is 0.424 nm with a thermal expansion coefficient of $9.0 \times 10^{-6}/^{\circ}\text{C}$. These values are close to those of MgO. Epitaxial grown TiN thin films on (001) Si substrates due to domain matching have been reported. TiN films were grown on Si under high vacuum using a wide deposition temperature range from 400 to 800 °C. [Narayan J. *et al.*] It was revealed that TiN (001) epitaxially grows on (001) Si in a Volmer-Weber type 4-on-3 cube-on-cube mode below 600 °C; while the growth mode changes to a Stranski-Krastinov 5-on-4 cube-on-cube type at higher temperature. [Willmott P. R. *et al.*] During the initial stage of TiN film deposition, the excess titanium adsorbs oxygen on silicon to establish epitaxial growth. These epitaxial TiN



films could act as a good diffusion barrier between MgO and Si layers. In the present work, SBN/MgO/TiN/Si heterostructures were fabricated for waveguide applications. In this structure, TiN thin films act as a buffer layer as well as diffusion barrier. The MgO buffer layer laid on top of TiN is used to prevent the TiN layer from oxidization at higher temperature and ambient oxygen environment required by subsequent SBN deposition.

5.2 Fabrication and Characterization of SBN/MgO/TiN

Heterostructure on (001) Si Substrates

In this section, the pre-treatment of Si substrates, the deposition conditions and the processing parameters of the fabrication of SBN/MgO/TiN heterostructure on (001) Si substrates are introduced in detailed. Their structural and waveguiding properties measurements are also reported. Following this section, the effects of the MgO film thickness on the optical loss of SBN films are discussed.



5.2.1 Pre-Treatment of Si Substrates

In this project, we have deposited the SBN/MgO/TiN heterostructure on (001) Si substrates with an area of 10 mm × 20 mm as required by the optical loss measurement using prism coupler. The Si substrates were dipped into 5% HF acid for 15 minutes to remove the native oxide layer. Then, they were cleaned with acetone in an ultrasonic cleaner.

5.2.2 Fabrication of SBN/MgO/TiN Heterostructure on (001) Si Substrates

The SBN target was prepared by conventional solid state reaction process as described by other group. [Zhu J. *et al*] The MgO and TiN targets were commercial targets with purities of 99.9% and 99.5%, respectively. The distance between the target and the substrate was kept at 40 mm throughout the fabrication process. For the deposition of TiN and MgO films, the pressure of the chamber was pumped down to 5×10^{-5} Torr. The substrate temperature was kept at 650 °C. Laser operated at 10 Hz repetition rate was properly focused to produce an energy density of 5 J/cm². For the fabrication of SBN films, the



laser repetition rate of 10 Hz, energy density of 5 J/cm^2 , ambient oxygen pressure of 200 mTorr, and substrate temperature of $740 \text{ }^\circ\text{C}$ were employed. Deposition time of 10 minutes, 15 minutes and 50 minutes were used to deposit TiN, MgO and SBN films respectively. finally, the as-deposited films were post-annealed at $740 \text{ }^\circ\text{C}$ and 200 mTorr oxygen pressure for another 15 min and then cooled down to room temperature naturally.

The structural properties and surface morphology of the heterostructure were characterized by X-ray diffraction (XRD) and scanning electron microscopy (SEM), respectively. To determine the surface roughness of the films, atomic force microscopy (AFM) was employed. The waveguide properties of the heterostructure were measured by using a coupling prism technique.

5.2.3 Structural Characterization and Surface Morphology of the SBN/MgO/TiN/Si Heterostructure

Figure 5.1 shows the XRD θ - 2θ profile of the SBN/MgO/TiN/Si heterostructure. The lattice constants of TiN and MgO are 0.424 and 0.421 nm, respectively, and hence, their (002) peaks are almost at the same 2θ position. The SBN (001)



and (002) peaks were clearly observed in the figure, indicating that the SBN is of single phase with *c*-axis oriented tetragonal structure. The ω -scan rocking curves were used to gauge the orientation quality of the films. The full-width-at-half-maxima (FWHM) of the rocking curves of MgO/TiN (002) and SBN (002) peaks are 1.44° and 2.10° , respectively. As a comparison, the FWHM of the Si substrate is 0.22° due to our equipment limitation. The FWHM value of SBN (002) is larger than that of SBN films grown on single crystal MgO discussed in chapter 4 (FWHM= 0.66°). To verify the epitaxial growth of the films, ϕ scans of the SBN (221), MgO/TiN (111), and Si (111) were performed and the results are shown in Figure 5.2. It is revealed that the MgO/TiN (111) and Si (111) diffraction peaks are at the same ϕ angles. Each set of the peaks are separated by 90° showing the four-fold symmetry of the samples. These results indicate that the MgO/TiN films are epitaxially grown on Si substrates. On the other hand, the SBN (221) diffraction peaks show a 45° rotation between the planes of MgO/TiN and SBN. This is different from the observations we described in chapter 4. This might due to the different processing temperature during the SBN deposition. From the ϕ scans data, the in-plane orientation relationship between the SBN films, MgO/TiN layers and Si substrates can be described as (110) SBN \parallel (100) MgO/TiN \parallel (100) Si.

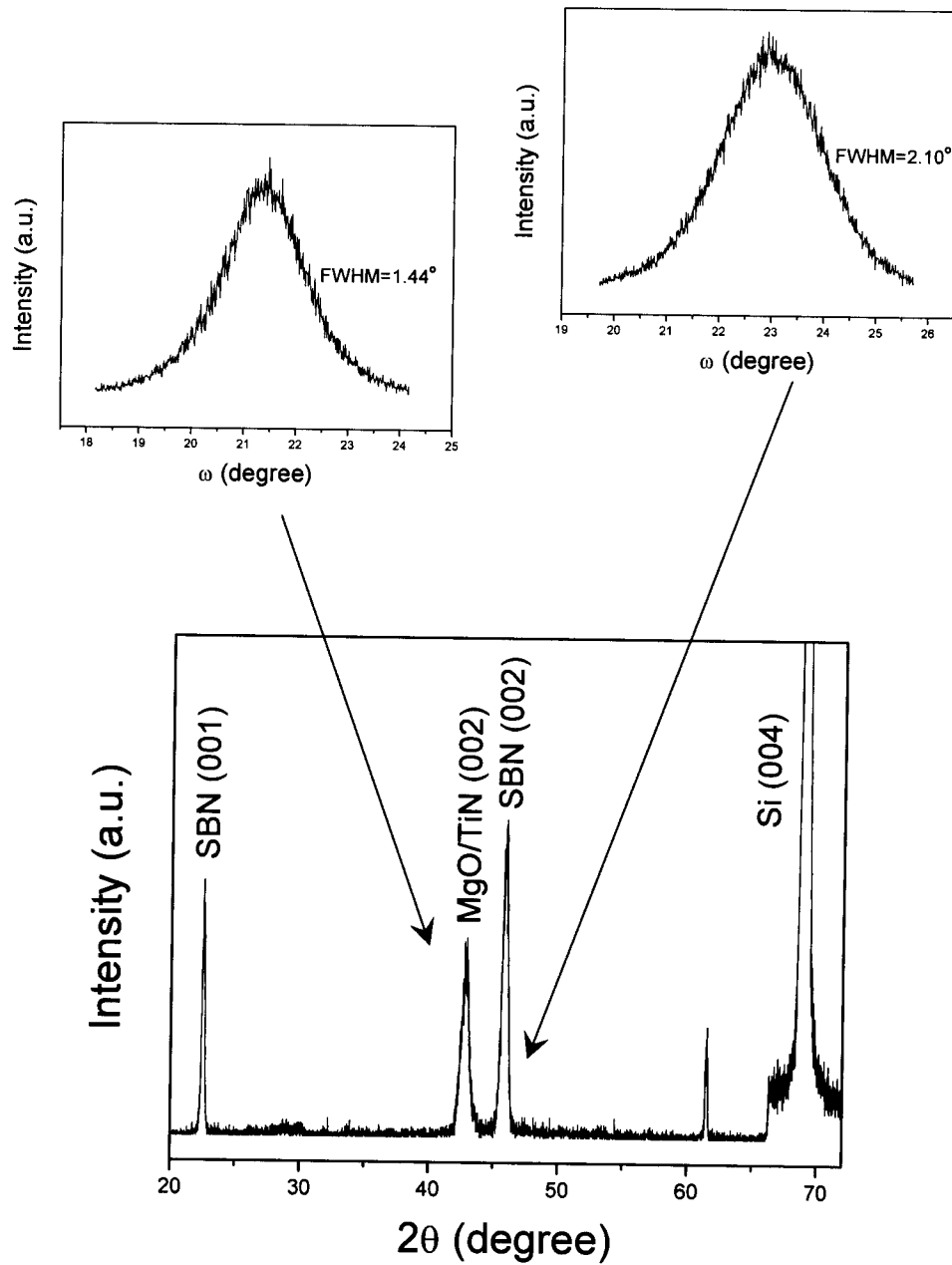


Figure 5.1 θ - 2θ scan patterns of the SBN/MgO/TiN heterostructure deposited on (001) Si substrates. The topmost figures show the rocking curves of SBN (200) and MgO/TiN peaks.

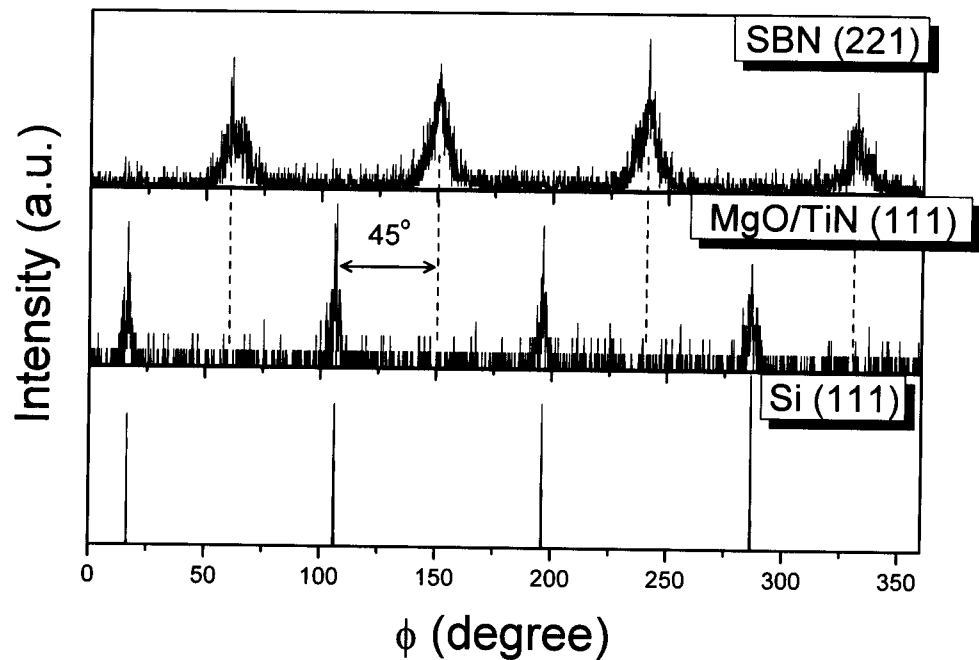


Figure 5.2 The X-ray diffraction ϕ scan profiles on the planes of Si (111),
MgO/TiN (111) and SBN (221)

The SEM micrographs in Figure 5.3 display the surface and cross-section morphologies of the heterostructure. The top layer surface micrograph shows a smooth, dense and crack-free surface, indicating the good surface quality of our films. From the cross-section micrograph, three prominent layers with columnar structures on top of the substrate are clearly identified. The thicknesses of the SBN, MgO and TiN layers are estimated to be 1 μ m, 200 nm



and 120 nm, respectively. The surface roughness was determined by AFM as shown in Figure 5.4. The root-means-square roughness is ~ 3.2 nm over a scanning area of $5 \mu\text{m} \times 5 \mu\text{m}$.

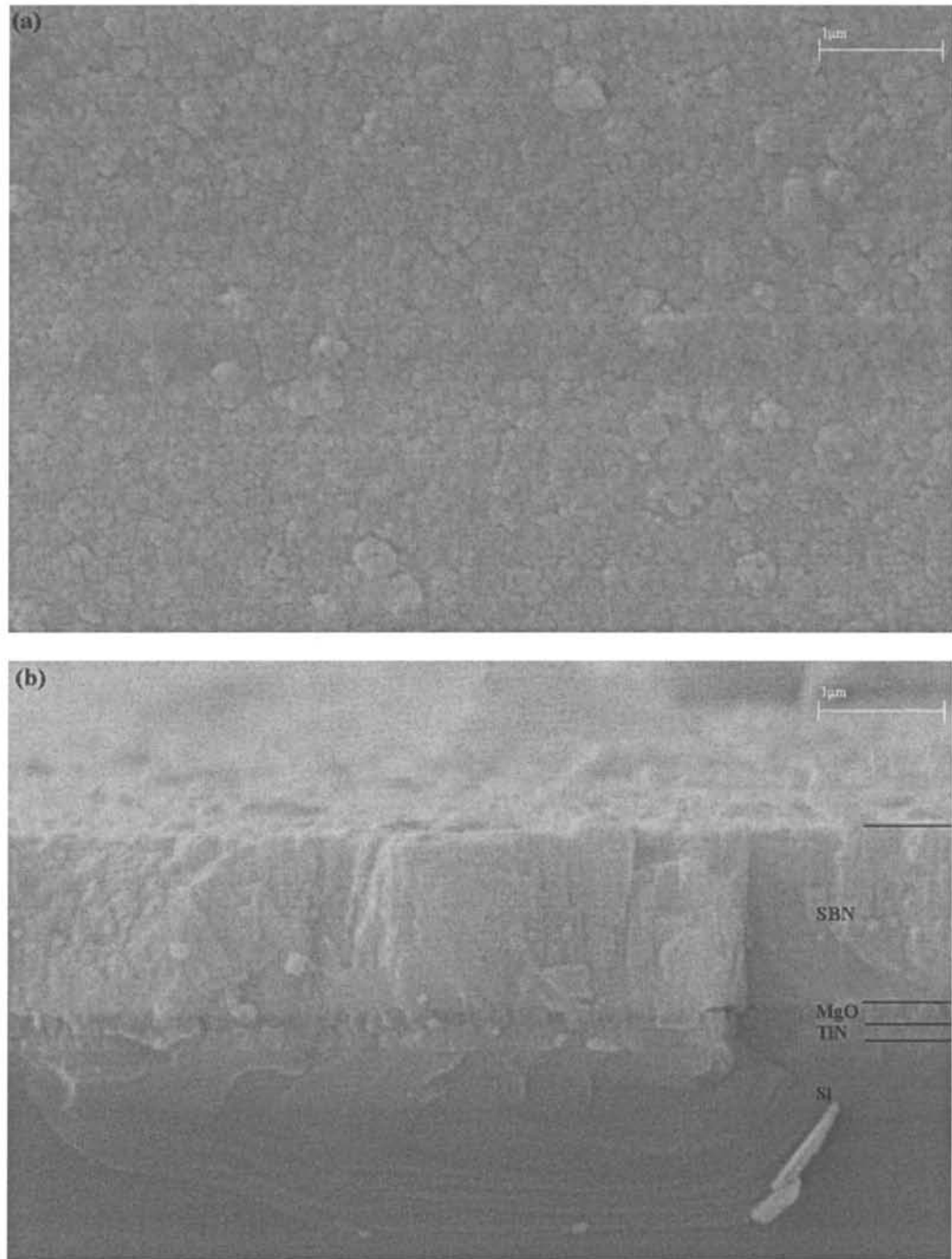


Figure 5.3 The SEM (a) surface and (b) cross-section micrographs of SBN/MgO/TiN heterostructure grown on (001) Si substrates

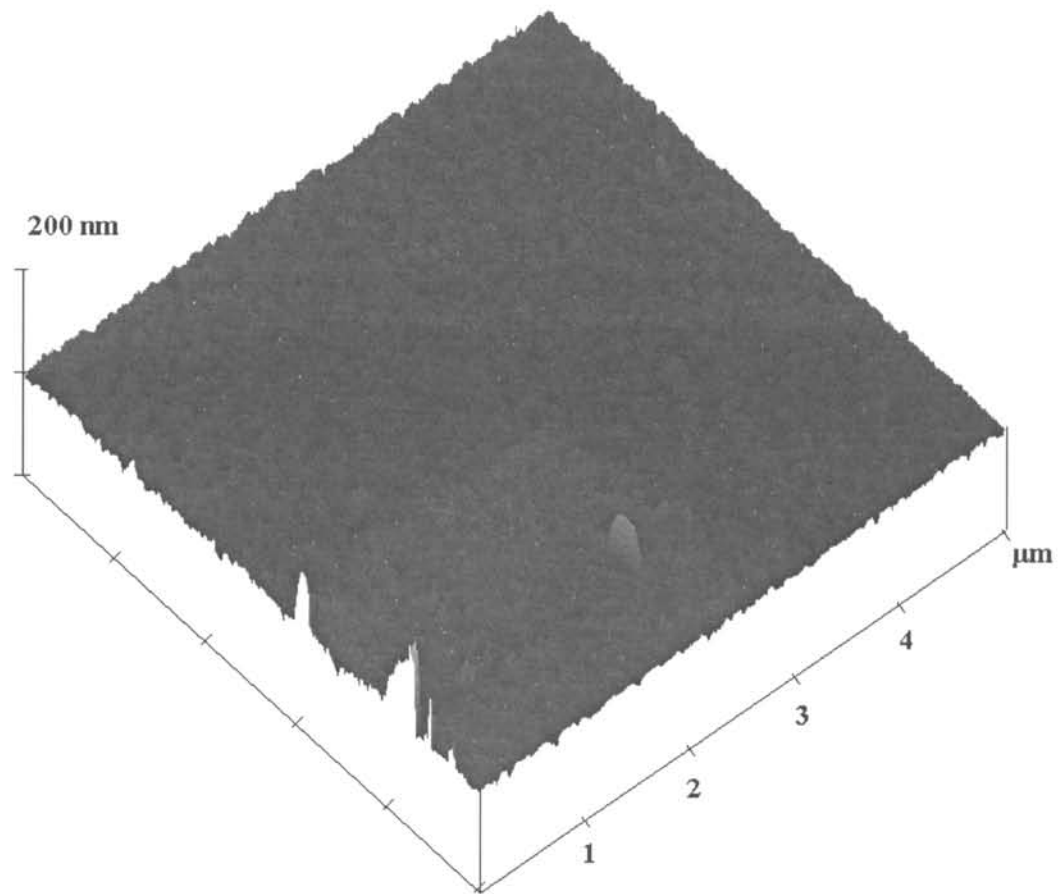


Figure 5.4 AFM image of SBN films deposited on MgO/TiN buffered (001) Si substrates

5.2.4 Waveguiding Properties Measurement of the Heterostructure by Coupling Prism Technique

A prism coupler operating at 632.8 nm was performed in order to characterize the waveguide properties of SBN/MgO waveguides grown on TiN buffered



(001) Si substrates. Figure 5.5 shows the guiding mode spectra (*m*-line) of SBN film with thickness of about 600 nm. In the figure, three TE (transverse electric) and three TM (transverse magnetic) modes are observed. All of the mode-lines are sharp and distinguishable, indicating that a good confinement of light propagation has been achieved and the film is a potential candidate for optical waveguide devices applications. The basic theory of coupling prism technique has been described in chapter 4. From our measured data, the ordinary refractive index n_o (n_{TE}) and the extraordinary refractive index n_e (n_{TM}) of SBN film were calculated to be 2.0393 and 2.0025, respectively. The thicknesses were calculated to be 914 nm and 1.12 μm . These values of thickness were in a good agreement with our SEM results. Both of the refractive indices are smaller than those of bulk SBN ($n_o = 2.312$ and $n_e = 2.281$). This deterioration of the refractive indices might be due to a much lower density of our SBN films as compared to that of SBN single crystal, which is partially resulted from the fast growth rate of our films. Therefore, we suggest that a lower laser energy and thus a slower growth rate should be employed in order to fabricate high quality SBN films.

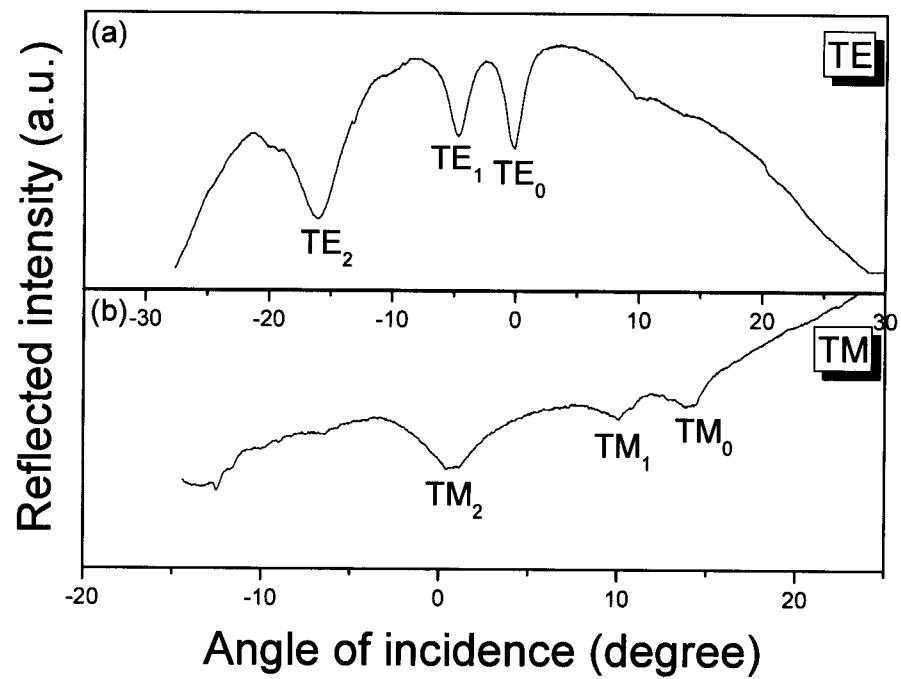


Figure 5.5 The (a) TE-line and (b) TM-line spectra for the air/SBN/MgO waveguide structure in the SBN/MgO/TiN/Si heterostructure.



5.3 Effects of the Film Thickness of MgO Layer on the Optical

Loss of the SBN Films

General speaking, a guided wave will leak through the cladding layer (MgO) into the substrate (Si) because the refractive index of Si is larger than that of the waveguiding layer. In order to decrease the leakage to an acceptable value, the thickness of the MgO layer must be chosen such that its value is sufficiently larger than the penetration depth of the guided wave. The minimum MgO thickness depends on the refractive index, thickness of the waveguide film, the wavelength and the mode of the guided wave. Hence, these parameters must be specified before the MgO thickness to be determined. Figure 5.6 shows the calculated minimum SiO₂ thickness required for TE₀ mode leakage-loss of less than 0.1dB/cm in SiO₂ buffered waveguide structure on Si substrates. In this project, to minimize the optical loss, the MgO thickness employed for TE₀ mode was estimated to be 500 nm for 1 μm thick SBN guided layer. The detailed relationship of the thickness of MgO layer and the optical loss of SBN films are being under investigation. A series of heterostructures buffered by MgO layer of different thicknesses is being fabricated.

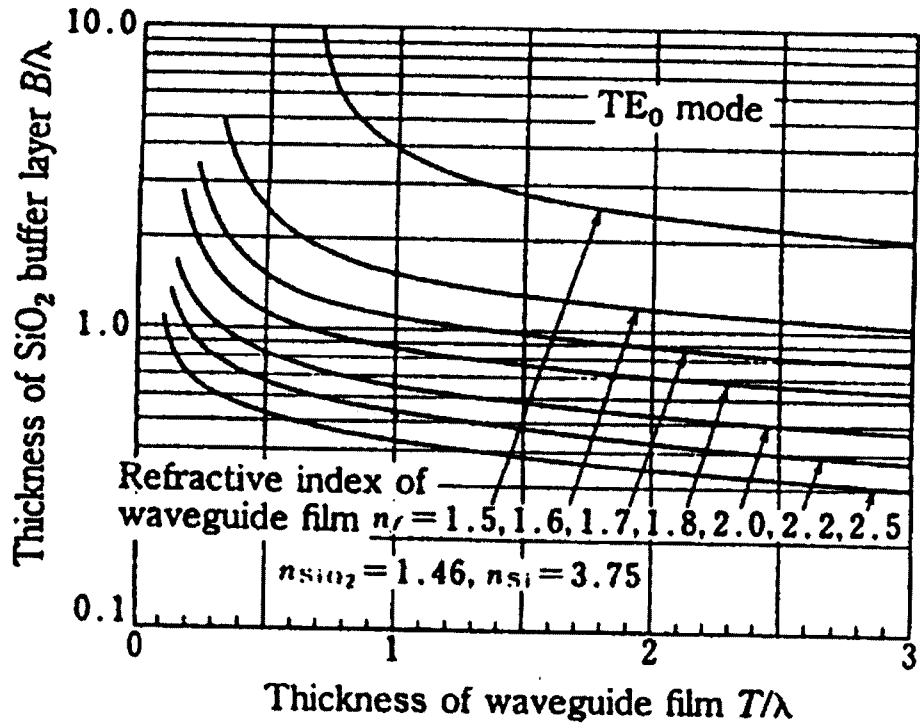


Figure 5.6 Minimum SiO₂ buffer layer thickness required to reduce the leakage loss of waveguides on SiO₂/Si substrate to 0.1dB/cm [Hiroshi Nishihara *et al*]



Chapter 6

Conclusions and Future Works

6.1 Conclusions

$\text{Li}_x\text{Ni}_{1-x}\text{O}$ (LNO) films with $x = 0.15, 0.20, 0.25, 0.30, 0.40, 0.50$ and 0.60 have been successfully fabricated on (001) MgO substrates by PLD. Above the deposition temperature of $600\text{ }^\circ\text{C}$, all of the LNO films exhibited epitaxially growth with single phase. They were c -axis oriented with cubic structure while some weak peaks identified as the Li_2O phase were observed from the profiles of LNO50 and LNO60 films. The LNO films were cube-on-cube grown on MgO substrates with an in-plane epitaxial relationship of (001) LNO || (001) MgO. XPS results showed that Li contents of the films were proportional to the initial Li contents. Indeed, the Li contents of the films were only approximately 20% of the corresponding initial Li contents. This is mainly due to the Li-evaporation during the deposition process. The surface morphology and film thickness were obtained from the SEM micrographs. The LNO films with different Li contents showed no remarkable difference in the shapes of their



optical transmittance spectra. A transmittance of about 40% in the visible range was obtained from LNO40 films. The optical band-gap energy of LNO was found to be in the range of 3.16~3.21 eV. Refractive index of the LNO films was determined to be about 1.75-2.0 by spectroscopic ellipsometry. The lowest resistivity was obtained in the LNO40 film deposited at 600 °C. Based on this consideration, LNO40 films were used in this project.

SBN films, which have been epitaxially grown on LNO buffered MgO substrates, showed a single phase cubic structure with *c*-axis orientation. In the fabrication of the SBN films, a two-step PLD deposition process was used in order to suppress the Li-evaporation at the high deposition temperature required by SBN deposition. With the LNO films being cube-on-cube grown on MgO substrates, epitaxial relationships of (100) SBN || (310) LNO/MgO and (100) SBN || (350) LNO/MgO were obtained. The surface morphology and film thickness were obtained by SEM. The optical transmittance and resistivity measurements indicated that our two-step PLD process can efficiently increase the transmission of the LNO films from 40% to 65% in the visible range meanwhile their resistivity was only slightly enhanced. The TE and TM guided modes of SBN films deposited on MgO substrates were measured by a



coupling prism technique. The ordinary refractive index n_o (n_{TE}) and the extraordinary refractive index n_e (n_{TM}) of SBN film were calculated to be 2.1843 and 2.1684, respectively, which are smaller than the values of bulk SBN probably due to a lower density of our SBN films as compared to that of SBN single crystal. At the same time, the thickness of SBN films obtained by the coupling prism technique was in a good agreement with our SEM results. A propagation loss of 3.45dB/cm was determined. We suggest that the waveguide properties can be improved by optimizing the deposition conditions as well as the processing parameters.

The SBN films were grown on (001) Si substrates by PLD using MgO/TiN as the buffer layers. The MgO/TiN and SBN films were single phase with c -axis orientation. They had cubic and tetragonal structures, respectively. All of the films were grown with cube-on-cube mode and the in-plane orientation relationship between the SBN films, MgO/TiN layers and Si substrates can be described as (110) SBN || (100) MgO/TiN || (100) Si. The SEM micrographs revealed the surface morphology and film thickness. The waveguide properties were measured by using a prism coupler. The ordinary refractive index n_o (n_{TE}) and the extraordinary refractive index n_e (n_{TM}) of SBN film were calculated to



be 2.0393 and 2.0025, respectively. These values were quite small as compared with that of SBN single crystal. It might be due to the fact that the films were grown too fast resulting in a lower film density of our SBN films. The relationship between the thickness of MgO layer and the propagation loss of SBN waveguide layer is under investigation.

Our preliminary researches studied a new family of waveguides with high electro-optical properties. It will assist the development of a new type of waveguide structures for future microelectronic device applications.

6.2 Future Works

In chapter 5, we have discussed that the thickness of MgO layer is a very important factor in determining the propagation loss of SBN waveguide films.

We suggest that heterostructures with MgO films of different thicknesses should be deposited in order to investigate the relationship between the MgO films thickness and the propagation loss of SBN films. The processing parameters of LNO and SBN/LNO films deposition should be varied in order to find the optimum conditions for the fabrication of the films with the best



optical transmittance and electrical conductivities at the same time. Although we have fabricated SBN films on MgO/TiN buffered Si substrates successfully by PLD methods, more suitable deposition conditions and operating parameters would be needed in order to obtain films with better surface and interface quality required by waveguide applications. In addition, a fabrication technique that combines PLD and sol-gel methods will be of interest to fabricate the samples. This method has been successfully used to fabricate epitaxial SBN films with thickness of above 1 μm in our group. The structural and optical properties of samples fabricated by this hybrid technique will be investigated in order to confirm whether the films prepared by this technique are suitable to be used in waveguide devices.

In the future, the effects of the processing parameters on the electro-optic (EO) properties in the SBN waveguide should be studied. The measurement of the EO coefficient r_{33} requires the application of an electrical field along the direction of c -axis. It is not possible to deposit electrodes on both sides of the film and to apply an E field that is parallel to the c -axis because our SBN film was deposited on MgO substrate which is insulating. This problem can be resolved by using a reflection-grating measurement technique [Trivedi D. *et al*]. As shown in Figure

6.1, planar interdigitated electrodes will be deposited on the top surface of the SBN film to induce a normal-direction E field. Input light is reflected from the grating to create a far-field diffraction pattern and a modulation of the refractive index, Δn , due to the linear electro-optic effect is induced when a voltage is applied upon the electrodes. The far-field diffraction pattern caused by the grating is affected by the extent of the modulation, Δn , which is proportional to the applied voltage. The change in the far-field intensity pattern is measured by modulating the applied voltage and measuring the change in the total optical power ΔP in the first order diffracted spot using a silicon photodetector and a lock-in amplifier. By relating the relative change in total optical power, $\Delta P/P$, in the first diffracted order and applied voltage, we can calculate the values of r_{33} as well as r_{13} .

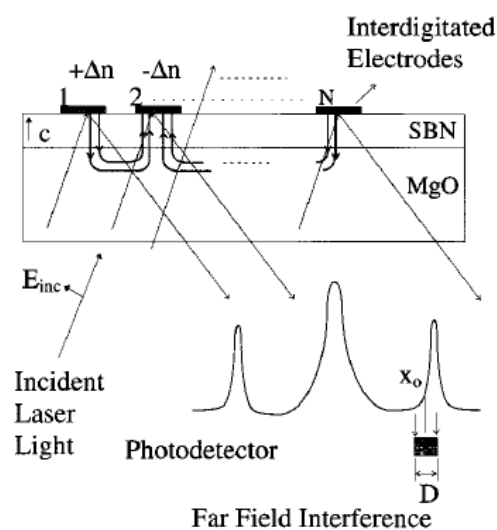


Figure 6.1 Schematic diagram of reflection-grating technique [Trivedi D. *et al*]



References

Adams M. J., *An Introduction to Optical Waveguides*, (John Wiley & Sons)

1981

Amnon Yariv and Pochi Yeh, *Photonics: Optical Electronics in Modern*

Communications, (Oxford University Press) 2007 Sixth Edition

Antolini E. and Ferretti M., *Mat. Lett.*, **30** (1997) 59-63

Antolini E., *Mat. Chem. & Phys.*, **52** (1998) 152-156

Antolini E. *Mat., Chem. & Phys.*, **82** (2003) 937-948

Azzoni C. B., Paleari A., Massarotti V., Bini M. and Capsoni D., *Phys. Rev. B*,

53 2 (1996) 703-709

Azzoni C. B., Paleari A., Massarotti V. and Capsoni D., *J. Phys.: Condens.*

Matter., **8** (1996) 7339-7347

Beckers L., Schubert J., Zander W., Ziesmann J., Eckau A. and Leinenbach P., *J.*

Appl. Phys., **83** 6 (1998) 3305-3310

Brice J. C., Hill O. F., Whiffin P. A. C. and Wilkinson J. A., *J. Cryst. Growth*,

10 (1971) 133-138

Cantoni C., Christen D. K., Varela M., Thompson J. R., Pennycook S. J.,

Specht E. D. and Goyal A., *J. Mat. Res.*, **18** 10 (2003) 2387-2400



- Chen T. L., Li X. M., Yu W. D. and Zhang X., *Appl. Phys. A*, **81** (2005)
657-661
- Chen X. Y., Wong K. H., Mak C. L., Liu J. M., Yin X. B., Wang M. and Liu Z.
G., *Appl. Phys. A*, **74** (2002) 703-706
- Chen X. Y., Wong K. H., Mak C. L., Yin X. B., Wang M., Liu J. M. and Liu Z.
G., *J. Appl. Phys.*, **91** 9 (2002) 5728-5734
- Chiu K. F. J., *Electrochem. Soc.*, **151** 11 (2004) A1865-A1869
- Chiu T-W, Wakiya N., Shinozaki K. and Mizutani N., *Thin Solid Films* **426**
(2003) 62-67
- Davis E. A., Mott N. F., *Philos. Mag.*, **22** (1970) 903-922
- Donald L. Smith, *Thin-Film Deposition: Principles & Practice*, (McGraw-Hill,
Inc) 1995
- Douglas B. Chrisey and Graham K. Hubler, *Pulsed Laser Deposition of Thin
Films*, (John Wiley & Sons, Inc) 1994
- Fujimori A. and Minami F., *Phys. Rev. B*, **30** 2 (1984) 957-971
- Guo X. L., Liu Z. G., Chen X. Y., Zhu S. N., Xiong S. B., Hu W. S. and Lin C.
Y., *J. Phys. D: Appl. Phys.*, **29** (1996) 1632-1635
- Gurumurugan K., Mangalaraj D., Narayandass S. K., Sekar K. and Vallabhan C.
P. G., *Semicond. Sci. Technol.*, **9** (1994) 1827-1832



- Haertling G. H., *J. Am. Ceram. Soc.*, **84** 4 (1999) 797-818
- He T., Ehrhart P. and Meuffels P., *J. Appl. Phys.*, **79** 6 (1996) 3219-3223
- Ho M. M.T., Mak C. L. and Wong K. H., *J. Euro. Ceram. Soc.*, **19** (1999)
1115-1118
- James D. Rancourt, *Optical Thin Films: User's Book*, (McGraw-Hill publishing
Company) 1987
- Jamieson P. B., Abrahams S. C. and Bernstein J. L., *J. Chem. Phys.*, **48** (1968)
5048-5057
- Jeggio C. R. and Boyd G. D., *J. Appl. Phys.*, **41** (1970) 2741-2743
- Kamiya T., Ohta H., Kamiya M., Nomura K., Ueda K., Hirano M. and Hosono
H., *J Mat. Res.*, **19** 3 (2004) 913-920
- Kapany N. S. and Burke J. J., *Optical Waveguides*, (Academic Press) 1972
- Lee M. K., Feigelson R. S., *J. Cryst. Growth.*, **180** (1997) 220-228
- Li A-D, Mak C. L., Wong K. H., Wu D. and Ming N. B., *J. Mat. Res.*, **16** 11
(2001) 3179-3183
- Li A-D, Mak C. L., Wong K. H., Ho M. M. T., Tang T. B., Yeung K. M., Wu D.
and Yang S-Z, *Jpn. J. Appl. Phys.*, **41** (2002) 6806-6809
- Li W., Reimers J. N. and Dahn J. R., *Phys. Rev. B*, **46** 6 (1992) 3236-3246
- Li Z. C., Wang C. W., Ma X. L., Yuan L. J. and Sun J. T., *Mat. Chem. & Phys.*,



91 (2005) 36-39

Lovell M. C., Avery A. J. and Vernon M. W., *Physical Properties of Materials*,

(English Language Book Society and van Nostrand Reinhold Co. Ltd.) 1976

Lu C-H. and Lee W-C., *J. Mat. Chem.*, **10** (2000) 1403-1407

Lu S. G., Mak C. L. and Wong K. H., *J. Am. Ceram. Soc.*, **84** 1 (2001) 79-84

Lu S. G., Mak C. L. and Wong K. H., *J. Appl. Phys.*, **94** 5 (2003) 3422-3426

Lu S. G., Zhu X. H., Mak C. L. Wong Y. H. Chan H. L. W. and Choy C. L., *Mat.*

Chem. & Phys., **79** (2003) 164-168

Lu S. G., Mak C. L., Wong K. H. and Cheah K. W., *Appl. Phys. Lett.*, **79** 26

(2001) 4310-4312

Luk C. H., Mak C. L. and Wong K. H., *Thin Solid Films*, **298** (1997) 57-61

Luk C. H., Ho M. M.T., Mak C. L., Wong K. H. and Pang G. K. H., *J. Euro.*

Ceram. Soc., **19** (1999) 1443-1446

Mak C. L., Lai B. and Wong K. H., *J. Sol-gel Sci. & Technol.*, **18** (2000)

225-233

Marini A., Massarotti V., Berbenni V., Capsoni D., Riccardi R., Antolini E. and

Passalacqua B., *Solid State Ionics*, **45** (1991) 143-155

Marx J. M., Tang Z., Eknoyan O., Taylor H. F. and Neurgaonkar R. R., *Appl.*

Phys. Lett., **66** (1995) 274-276



- Megumi K., Nagatsuma N., Kashiwada Y. and Furuhearta Y., *J. Mat. Sc.*, **11**
(1976) 1583-1592
- Mendes R. G., Araújo E. B. and Eiras J. A., *J. Phys.: Condens. Matter.*, **11**
(1999) 9611-9617
- Mendes R. G., Araújo E. B. and Eiras J. A., *Mat. Res.*, **4** 2 (2001) 113-116
- Michalak F., von Rottkay K., Richardson T., Slack J. and Rubin M.,
Electrochimica Acta, **44** 18 (1999) 3085-3092
- Nystrom M. J., Wessels B. W., Neumayer D. A. and Marks T. J., *Appl. Phys.*
Lett., **66** 14 (1995) 1726-1728
- Pickering I. J., Lewandowski J. T., Jacobson A. J. and Goldstone J. A., *Solid*
State Ionic, **53-56** (1992) 405-412
- Puspharajah P., Radhakrishna S. and Arof F.K., *J. Mat. Sci.*, **32** (1997)
3001-3006
- Qu Y. Q., Li A-D., Shao Q. Y., Tang Y. F., Wu D., Mak C. L., Wong K.H. and
Ming N. B., *Mat. Res. Bull.*, **37** (2002) 503-513
- Reimers Jan N., Li W. and Dahn J. R., *Phys. Rev. B*, **47** 14 (1993) 8486-8497
- Richard Syms and John Cozens, *Optical Guided Waves and Devices*,
(McGraw-Hill Book Company) 1992
- Rougier A., Chadwick A. V. and Delmas C., *Nuclear Instruments and Methods*



in Physics Research B, **97** (1995) 75-77

Rougier A., Delmas C. and Chadwick A. V., *Solid State Communications*, **94** 2

(1995) 123-127

Rouleau C. M., Jellison G. E., Jr and Beach D. B., *Appl. Phys. Lett.*, **82** 18

(2003) 2990-2992

Rubin M., Wen S-J., Richardson T., Kerr J., von Rottkay K. and Slack J., *Solar Energy Materials & Solar Cells*, **54** (1998) 59-66

Rubin M., von Rottkay K., Wen S-J., Ozer N. and Slack J., *Solar Energy*

Materials & Solar Cells, **54** 1 (1998) 49-57

Sharma A. K., Kvit A. and Narayan J. J., *Vac. Sci. Technol. A*, **17** 6 (1999)

3393-3396

Stoyanova R., Zhecheva E. and Angelov S., *Solid State Ionics*, **59** (1993) 17-24

Tanaka K., Nakagawara O. Nakano M., Shimuta T., Tabata H. and Kawai T.,

Jpn. J. Appl. Phys., **37** (1998) 6142-6145

Tayebati P., Trivedi D. and Tabat M., *Appl. Phys. Lett.*, **69** 8 (1996) 1023-1025

Thöny S. S., Youden K. E. Harris JR J. S. and Hesselink L., *Appl. Phys. Lett.*,

65 16 (1994) 2018-2020

Tian H. Y., Choi J. W., No K., Luo W-G. and Ding A-L., *Mat. Chem. & Phys.*,

78 (2002) 138-143



- Trivedi D., Tayebati P. and Tabat M., *Appl. Phys. Lett.*, **68** 23 (1996) 3227-3229
- Tsang W. S., Chan K. Y., Mak C. L. and Wong K. H., *Appl. Phys. Lett.*, **83** 8
(2003) 1599-1561
- Tunyagi A. R., Ulex M. and Betzler K., *Phys. Rev. Lett.*, **90** (2003) 243901
- Ulrich R. and Torge R., *Appl. Opt.*, **12** 2 (1973) 2901-2908
- Van Elp J., Eskes H., Kuiper P. K. and Sawatzky G. A., *Phys. Rev. B*, **45** 4
(1992) 1612-1622
- Vasquez R. A., Ewbank M. D. and Neurgaokar R. R., *Opt. Comm.*, **80** (1991)
253-258
- Wang D. Y., Chan H. L. W. and Choy C. L., *Appl. Opt.*, **45** 9 (2006) 1972-1978
- Wang H., Sharma A., Kvit A., Wei Q., Zhang X., Koch C. C. and Narayan J. J.,
Mat. Res., **16** 9 (2001) 2733-2738
- Wen S-J., von Rottkay K. and Rubin M., *Proc. Electrochem. Soc.*, **96** 24 (1997)
54-63
- Wen S-J., Kerr J., Rubin M., Slack J. and von Rottkay K., *Solar Energy
Materials & Solar Cells*, **56** (1999) 299-307
- White J. M. and Heidrich P. F., *Appl. Opt.*, **15** 1 (1976) 151-155
- Willmott P. R., Timm R., Huber J. R., *Appl. Surf. Sci.*, **127-129** (1998) 105-110
- Wu J., Nan C-W., Lin Y. H. and Deng Y., *Phys. Rev. Lett.*, **89** 21 (2002)



217601-1

Wu W. B., Wong K. H. and Choy C. L., *Thin Solid Films*, **360** (2000) 103-106

Xiong S. B., Ye Z. M., Chen X. Y., Guo X. L., Zhu S. N., Liu Z. G., Lin C. Y.

and Jin Y. S., *Appl. Phys. A.*, **67** (1998) 313-316

Xu X. Q., Ye H. and Zou T., *J. Zhengjing University Science A*, **7** 3 (2006)

472-476

Xu Y. H., Chen C. H., Xu R. and Mackenzie J. D., *Phys. Rev. B*, **44** (1991) 35-41

Youden K. E., Thöny S. S., Hesselink L. and Harris JR J. S., *Mat. Res. Soc. Symp.*

Proc., **361** (1995) 173-178

Zhang Y. L., Mak C. L. Wong K. H. and Choy C. L., *Thin Solid Films*, **449**

(2004) 63-66

Zheleva T., Jagannadham K. and Narayan J., *J. Appl. Phys.*, **75** (1994) 860-871

Zhu J., Singh S. K., Thomas P. A. and Palmer S. B., *Cryst. Res. Technol.*, **34** 9

(1999) 1205-1211

Zhu Y. Y., Xiao R. F. and Wong G. K. L., *J. Appl. Phys.*, **82** (1997) 4908-4911